Journal for ImmunoTherapy of Cancer

Multimodule characterization of immune subgroups in intrahepatic cholangiocarcinoma reveals distinct therapeutic vulnerabilities

Jian Lin ,[1] Yuting Dai,[2] Chen Sang,[3] Guohe Song,[3] Bin Xiang,[4] Mao Zhang,[3] Liangqing Dong,[3] Xiaoli Xia,[2] Jiaqiang Ma,[3] Xia Shen,[1] Shuyi Ji,[1] Shu Zhang,[3] Mingjie Wang,[5] Hai Fang,[2] Xiaoming Zhang,[6] Xiangdong Wang,[1] Bing Zhang,[7] Jian Zhou,[3,8] Jia Fan,[3,8] Hu Zhou ,[9] Daming Gao,[10] Qiang Gao[1,3,8]

To cite: Lin J, Dai Y, Sang C, *et al*. Multimodule characterization of immune subgroups in intrahepatic cholangiocarcinoma reveals distinct therapeutic vulnerabilities. *Journal for ImmunoTherapy of Cancer* 2022;**10**:e004892. doi:10.1136/jitc-2022-004892

► Additional supplemental material is published online only. To view, please visit the journal online (http://dx.doi.org/10.1136/jitc-2022-004892).

JL, YD, CS, GS and BX contributed equally.

Accepted 01 July 2022

For numbered affiliations see end of article.

Correspondence to
Dr Qiang Gao;
gaoqiang@fudan.edu.cn

Dr Daming Gao;
dgao@sibcb.ac.cn

Dr Hu Zhou;
zhouhu@simm.ac.cn

ABSTRACT

Background Immune microenvironment is well recognized as a critical regulator across cancer types, despite its complex roles in different disease conditions. Intrahepatic cholangiocarcinoma (iCCA) is characterized by a tumor-reactive milieu, emphasizing a deep insight into its immunogenomic profile to provide prognostic and therapeutic implications.

Methods We performed genomic, transcriptomic, and proteomic characterization of 255 paired iCCA and adjacent liver tissues. We validated our findings through H&E staining (n=177), multiplex immunostaining (n=188), single-cell RNA sequencing (scRNA-seq) (n=10), *in vitro* functional studies, and *in vivo* transposon-based mouse models.

Results Integrated multimodule data identified three immune subgroups with distinct clinical, genetic, and molecular features, designated as IG1 (immune-suppressive, 25.1%), IG2 (immune-exclusion, 42.7%), and IG3 (immune-activated, 32.2%). IG1 was characterized by excessive infiltration of neutrophils and immature dendritic cells (DCs). The hallmark of IG2 was the relatively higher tumor-proliferative activity and tumor purity. IG3 exhibited an enrichment of adaptive immune cells, natural killer cells, and activated DCs. These immune subgroups were significantly associated with prognosis and validated in two independent cohorts. Tumors with *KRAS* mutations were enriched in IG1 and associated with myeloid inflammation-dominated immunosuppression. Although tumor mutation burden was relatively higher in IG2, loss of heterozygosity in human leucocyte antigen and defects in antigen presentation undermined the recognition of neoantigens, contributing to immune-exclusion behavior. Pathological analysis confirmed that tumor-infiltrating lymphocytes and tertiary lymphoid structures were both predominant in IG3. Hepatitis B virus (HBV)-related samples tended to be under-represented in IG1, and scRNA-seq analyses implied that HBV infection indeed alleviated myeloid inflammation and reinvigorated antitumor immunity.

Conclusions Our study elucidates that the immunogenomic traits of iCCA are intrinsically heterogeneous among patients, posing great challenge and opportunity for the application of personalized immunotherapy.

WHAT IS ALREADY KNOWN ON THIS TOPIC

⇒ Intrahepatic cholangiocarcinoma (iCCA) represents the second most common type of primary liver cancer, which is generally featured by a highly desmoplastic tumor microenvironment (TME). Sequencing efforts have improved the understanding of the molecular pathogenesis of iCCA; however, the comprehensive landscape of iCCA microenvironment phenotype remains largely unexplored.

WHAT THIS STUDY ADDS

⇒ Our multimodule study reveals three distinct immune subgroups (IG1, IG2, and IG3) with specific immunological and non-immune profiles associated with different patient outcomes. Myeloid inflammation/*KRAS* mutation, antigen presentation/proliferation, and immune checkpoint could serve as potential therapeutic targets for the treatments of IG1, IG2, and IG3-related iCCA, respectively. Hepatitis B virus (HBV) infection could probably alleviate myeloid inflammation in iCCA, thus activates antitumor immunity and improves the efficacy of immunotherapies.

HOW THIS STUDY MIGHT AFFECT RESEARCH, PRACTICE OR POLICY

⇒ These findings extend our understanding of the immunological profile of iCCA. Defined immune subgroups provide novel insights into the heterogeneous TME and underlying therapeutic strategies.

INTRODUCTION

Intrahepatic cholangiocarcinoma (iCCA) accounts for 10%–15% of all primary liver cancer, with a gradual increase over the past decades.[1] Despite the high postoperative recurrence rate, surgery is prior for patients diagnosed at an early stage. Unfortunately,

most patients are diagnosed at advanced stages, when only palliative chemotherapy is available, with a median survival shorter than 12 months. Emerging molecular targeted therapies against *FGFR2* fusion and *IDH1/2* mutations show modest survival benefits in a limited subgroup of patients with iCCA.[2] Hence, identification of novel and effective therapeutics remains an urgent need.

In general, iCCA is featured by a highly desmoplastic tumor microenvironment (TME) with excessively infiltrating immune and stromal cells. Available evidence indicates that the inflammatory microenvironment is associated with iCCA progression and poor prognosis,[3] highlighting TME as a potential target for the treatment of iCCA. Indeed, recent phase II/III clinical trials confirm that immune checkpoint inhibitors (ICIs) plus chemotherapy is promising in patients with iCCA.[4 5] However, the responses and survival benefits are only limited to a small subset of patients, probably owing to the heterogeneous and complex TME. Therefore, a better understanding of the immunogenomic profile is urgently needed for designing novel immunotherapies to improve responses and patient outcomes.

Patient stratification based on immune profile can help delineate immunologically heterogeneous tumors and identify suitable patients for immunotherapy.[6 7] We and others have applied bulk-tumor transcriptomic or proteomic profiles to define clinically relevant iCCA subtypes,[8–13] collectively converging on intertumor immune heterogeneity. Nevertheless, the underlying cancer-cell-intrinsic properties that dictate the diversity in immune landscape remain less characterized. Integrated multidimensional and multimodule analyses of preclinical models and patient samples are needed and expected to deeply characterize the immunological portraits and identify novel personalized immunotherapeutic opportunities in each molecular subtype of iCCA.

In this study, we analyzed the transcriptomic profiles of TME using the largest single-centered iCCA cohort and classified 255 patients into three immune subgroups (IG1, IG2, IG3). By integrating multiple complementary approaches, including whole-exome sequencing (WES), proteomics, single-cell RNA sequencing (scRNA-seq), immunostaining, and mouse models, we delineated the distinct genetic and molecular features among these subgroups. IG1 was an immune-suppressed subgroup with the worst prognosis, harboring the highest myeloid infiltration and *KRAS* mutations; IG2 was characterized by tumor proliferation and antigen presentation defects; IG3 was featured by the activation of antitumor immunity and enrichment of tertiary lymphoid structures (TLSs), with a good prognosis. The substantial differences in immunological profile suggested that each immune subgroup need specific therapeutic strategies.

METHODS

The iCCA samples from 255 patients used for this study were collected from Zhongshan Hospital of Fudan University. Patients treated between December 2014 to October 2018 were randomly selected from our prospectively collected tissue bank. Detailed clinicopathological features are summarized in online supplemental table S1.

Full details of multi-omics analysis, multiplexed immunostaining of tissue microarray (TMA), pathological examination, mouse model construction, scRNA-seq analysis, functional experiments, and statistical analysis are provided in the online supplemental materials and methods.

RESULTS

Immune-centered classification of iCCA

To characterize the immune profile of iCCA with prognostic significance, multi-omics data derived from the Fudan University (FU-iCCA) cohort (n=255) were obtained (online supplemental figure S1A and online supplemental table S1).[11] Consistent with iCCA's inflammatory and desmoplastic features, our cohort had a relatively higher immune infiltration among The Cancer Genome Atlas (TCGA) Pan-Cancer datasets (online supplemental figure S1B). Unsupervised hierarchical clustering based on the mRNA levels of 170 prognostic genes from TME signature[14] revealed three Immune subGroups, namely IG1, IG2, and IG3 (figure 1A; online supplemental figure S1C–E and online supplemental table S1). Pairing the transcriptomic and proteomic data from this signature created 103 mRNA–protein pairs, which showed an overall positive correlation (median r=0.6, multiple-test adjusted p<0.01; online supplemental figure S1F). Of note, the abundance of corresponding 103 proteins also clustered these patients into similar immune subgroups with a comparable overlap (online supplemental figure S1G).

As expected, the immune subgroups significantly differed in overall survival (p=1e-09, log-rank test) and recurrence-free survival (p=4e-07, log-rank test), where IG1 had the worst and IG3 showed the best prognosis (figure 1B). Multivariable Cox analysis further authenticated the immune subgroups as a significantly independent prognosticator (HR, 2.4; 95% CI, 1.33 to 4.5; p=4e-03; figure 1C). Carbohydrate antigen 19-9 (CA19-9, p=6.8e-11) and carcinoembryonic antigen (CEA, p=1.2e-06) were significantly higher in IG1, whereas albumin (ALB, p=9.9e-03) levels increased gradually from IG1 to IG3 (online supplemental figure S1H). IG1 had more tumors with necrosis (p=0.012) and advanced tumor node metastases (TNM) stage (p=2.7e-04) (figure 1D and online supplemental figure S1H). Of note, lymph node metastasis (p=0.019) and vascular invasion (p=0.038) were predominated in IG1, whereas endothelial cells were enriched in IG3. Increased lymphangiogenesis and reduced angiogenesis could make iCCA more invasive and impair treatment efficacy.[15] Thus, immunostaining confirmed that compared with IG3, where extensive CD31+ blood vessels were observed, IG1 showed a marked

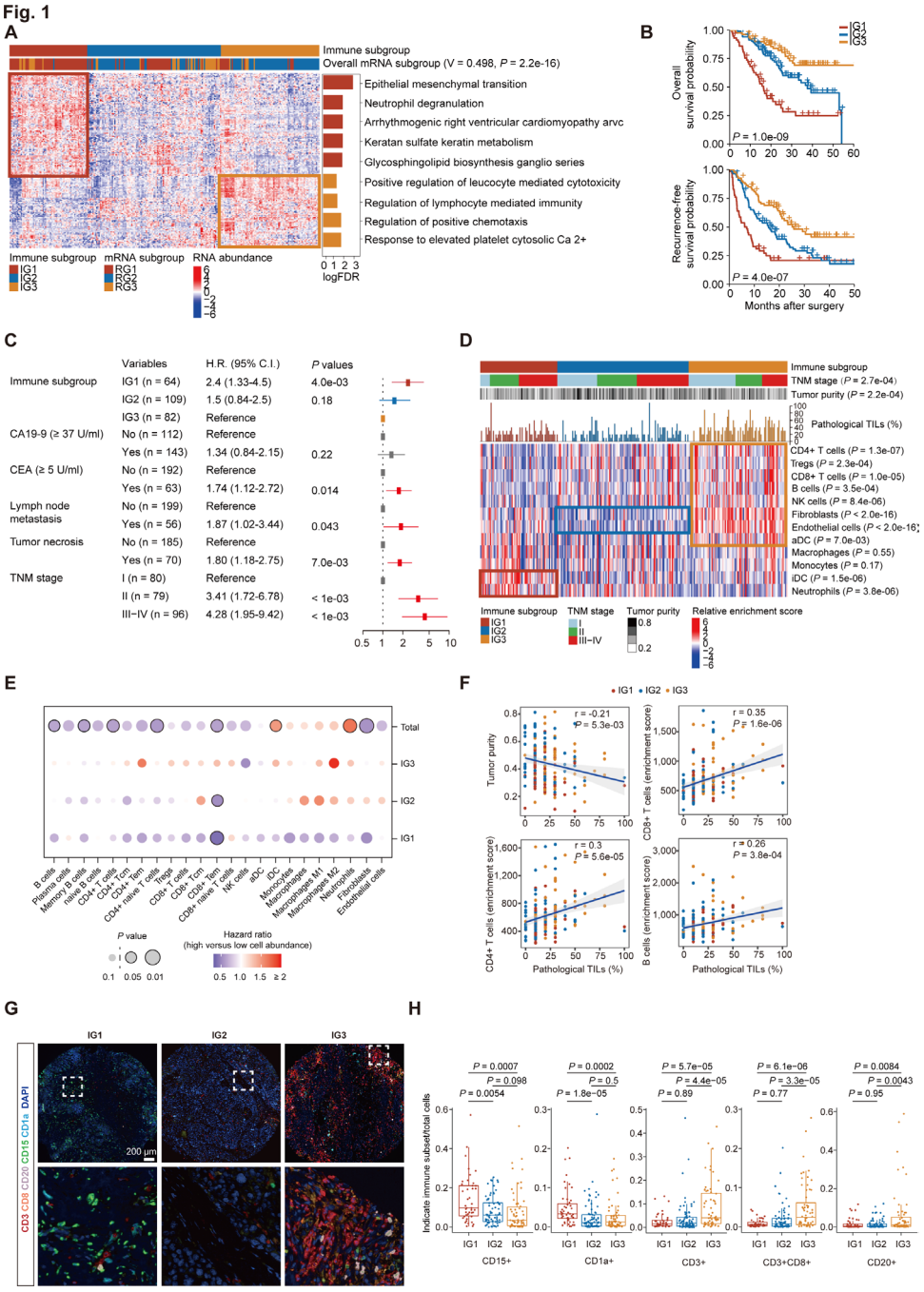

Figure 1 Immune-centered classification of intrahepatic cholangiocarcinoma (iCCA). (A) Unsupervised hierarchical clustering of the Fudan University (FU)-iCCA (n=255) cohort based on the 170 genes. The enriched pathways in IG1 and IG3 were shown on the right (χ^2 test and adjusted analysis of variance (ANOVA)). (B) Kaplan-Meier curves for overall survival (upper panel) and recurrence-free survival (bottom panel) among the three immune subgroups (log-rank test). (C) HR and p values of immune subgroups and covariates in multivariate analysis for overall survival. (D) The relative abundance of tumor microenvironment (TME) subsets identified from xCell (Fisher's exact test or ANOVA). (E) Univariate analysis for overall survival of each cell subset. (F) Pathological tumor-infiltrating lymphocyte (TIL) estimates (n=177) plotted for each tumor sample against indicated signatures. (G) Representative immunostaining images showing the indicated immune subsets. (H) Quantification of staining intensities for the indicated immune markers (n=188, ANOVA).

increase in podoplanin positive (PDPN+) lymphatic vessels (online supplemental figure S1I).

Within this prognostic TME signature, IG1 was enriched with pathways of neutrophil degranulation and epithelial–mesenchymal transition (EMT), suggesting an inflammatory and invasive phenotype. In contrast, leucocyte-mediated cytotoxicity and lymphocyte-mediated immunity pathways were predominant in IG3, indicating an immune-active milieu (figure 1A). As expected, xCell[14] deconvolution of the RNA-seq data showed that IG1 was dominant by myeloid cells such as neutrophils and immature DCs (iDC), whereas IG3 was abundant in adaptive

immune cells, natural killer (NK) cells, and activated DCs (aDC). Immune infiltration in IG2 was relatively low and heterogeneous, accompanied by the scarcity of stromal cells, which might account for the highest tumor purity (p=2.2e-04; figure 1D). Generally, the abundance of neutrophils (p=0.011) and iDC (p=0.045) predicted poor survival, whereas the accumulations of lymphocytes, such as CD4+ T cells, CD8+ T effector/memory (Tem) cells, and B cells, were associated with good prognosis (log-rank test; figure 1E).

Further pathological examination confirmed that tumors in IG3 contained more tumor-infiltrating lymphocyte (TIL) estimates (figure 1D; online supplemental figure S1J,K and online supplemental table S1). Indeed, TIL estimates correlated negatively with tumor purity (p=5.3e-03) and positively with immune deconvolution (CD8+ T, p=1.6e-06; CD4+ T, p=5.6e-05; B cell, p=3.8e-04; figure 1F). Similarly, multiplex immunostaining on TMAs confirmed that the intensities of CD15, CD66b, and CD1a were the strongest in IG1, whereas CD3, CD8, and CD20 were primarily expressed in IG3 (figure 1G and H; online supplemental figure 1L and online supplemental table S1), remarkably consistent with the xCell estimation.

We then performed unsupervised clustering based on the overall mRNAs with the top 25% median absolute deviation and identified three subgroups that were somehow concordant with the immune subgroups (figure 1A). Specifically, pairing immune subgroups and overall mRNA subgroups (RGs) showed that IG1 and IG3 highly overlapped with RG1 and RG2, respectively. Leveraging our TME gene signature, we also classified Jusakul *et al*'s and Job *et al*'s iCCA cohorts and observed similar patient subgrouping and survival stratification (online supplemental figure 2A–D). Likewise, clustering our RNA-seq data with the transcriptomic signatures from four previous studies[8–10 12] resulted in a significant concordant patient allocation (online supplemental figure 2E–H).

Distinct molecular features among the three immune subgroups

To further illustrate the key biological processes in patient subgroups, we performed single sample Gene Set Enrichment Analysis (GSEA) using the 50 hallmark gene sets[16] (online supplemental figure S3A and online supplemental table S2). Analysis of principal-component feature showed that PC1 could be explained by tumor purity with immune and stromal gene set vectors opposite to oncogenic and other vectors, whereas PC2 discriminated immune from stromal gene sets (online supplemental figure S3A–C). Unsupervised hierarchical clustering further verified the association between signaling pathways and immune subgroups, as well as separated clustering of immune and other gene sets (online supplemental figure S3D).

Pathway enrichment analysis incorporating both transcriptomics and proteomics data demonstrated distinct molecular features among the immune subgroups (figure 2A). IG1 was high in inflammatory response, interleukin 6 (IL-6)/janus kinase (JAK)/signal transducer and activator of transcription 3 (STAT3) signaling, and tumor necrosis factor-α (TNF-α)/nuclear factor kappa-B (NF-κB) signaling, indicating that these tumors may be driven by smoldering inflammation. Hypoxia and glycolysis pathways, which have been implicated in myeloid cell-mediated tumor immune evasions,[17 18] were also predominant in IG1. IG2 were characterized by enrichment of cell-cycle transcriptional programs (G2M checkpoint, E2F targets, Myc targets) and DNA repair pathway, demonstrating the high proliferative activity. Considering the highest tumor burden in IG2, we adjusted the tumor purity[19] and still found enriched proliferation-associated pathways in IG2 (online supplemental figure S3E and online supplemental table S2). IG3 was associated with downregulation of glycolysis and hypoxia pathways, as well as upregulation of the oxidative phosphorylation (OXPHOS) pathway, which has been highlighted as the critical aspects of immune activation[20] (figure 2A).

We further focused on cancer-promoting and cancer-inhibitory inflammation. IG1 was enriched in protumor inflammatory cytokines and chemokines, including IL-1A, IL-1B, IL-6, CXCL3, CXCL5, and CCL18 (figure 2B). The mRNA and protein levels of most S100A family members, including S100A8/A9, were upregulated in IG1, which may be involved in cancer-promoting inflammation[21] (figure 2C). Concurrently, increased mRNA and protein levels of CD8A, GZMA, and PRF1 confirmed the upregulation of cancer-inhibitory inflammation in IG3 (figure 2B). Moreover, a panel of immune signatures[18 22–24] collectively showed that IG3 displayed elevated T-cell survival and T-effector signatures relative to other subgroups, whereas IG1 exhibited elevated myeloid-derived suppressor cells (MDSC), M2/M1 macrophage, myeloid inflammation, and proinflammation signatures (figure 2D and online supplemental table S2). Overall, our stratification identified two immune subgroups with antagonistic inflammatory phenotypes.

Recently, the cyclooxygenase 2 (COX-2)/prostaglandin E2 (PGE2) axis has been reported to be involved in regulating the antagonistic inflammatory phenotypes in a Pan-Cancer study.[25] Indeed, the transcript levels of *PTGS2*, encoding for COX-2, were significantly upregulated in IG1 (figure 2B,E), consistent with the excessive infiltration of PGE2-associated neutrophils and iDCs.[26 27] As expected, patients with higher COX-2 mRNA levels had a worse prognosis (p=1e-04, log-rank test; figure 2F). Strong positive correlations between COX-2 mRNA levels and cancer-promoting factors[28] including IL-1A, IL-1B, and IL-6 were detected (figure 2G and online supplemental table S2). Infiltration of neutrophils and iDCs positively correlated with COX-2 mRNA level, whereas plasma cells, CD4+ T cells, and CD8+ Tem cells showed negative correlations (figure 2H and online supplemental table S2). The COX-2-associated inflammatory signature (COX-IS) was a predictor for response to ICIs in multiple cancers,[28] and COX-IS decreased sequentially from IG1 to IG3 (online

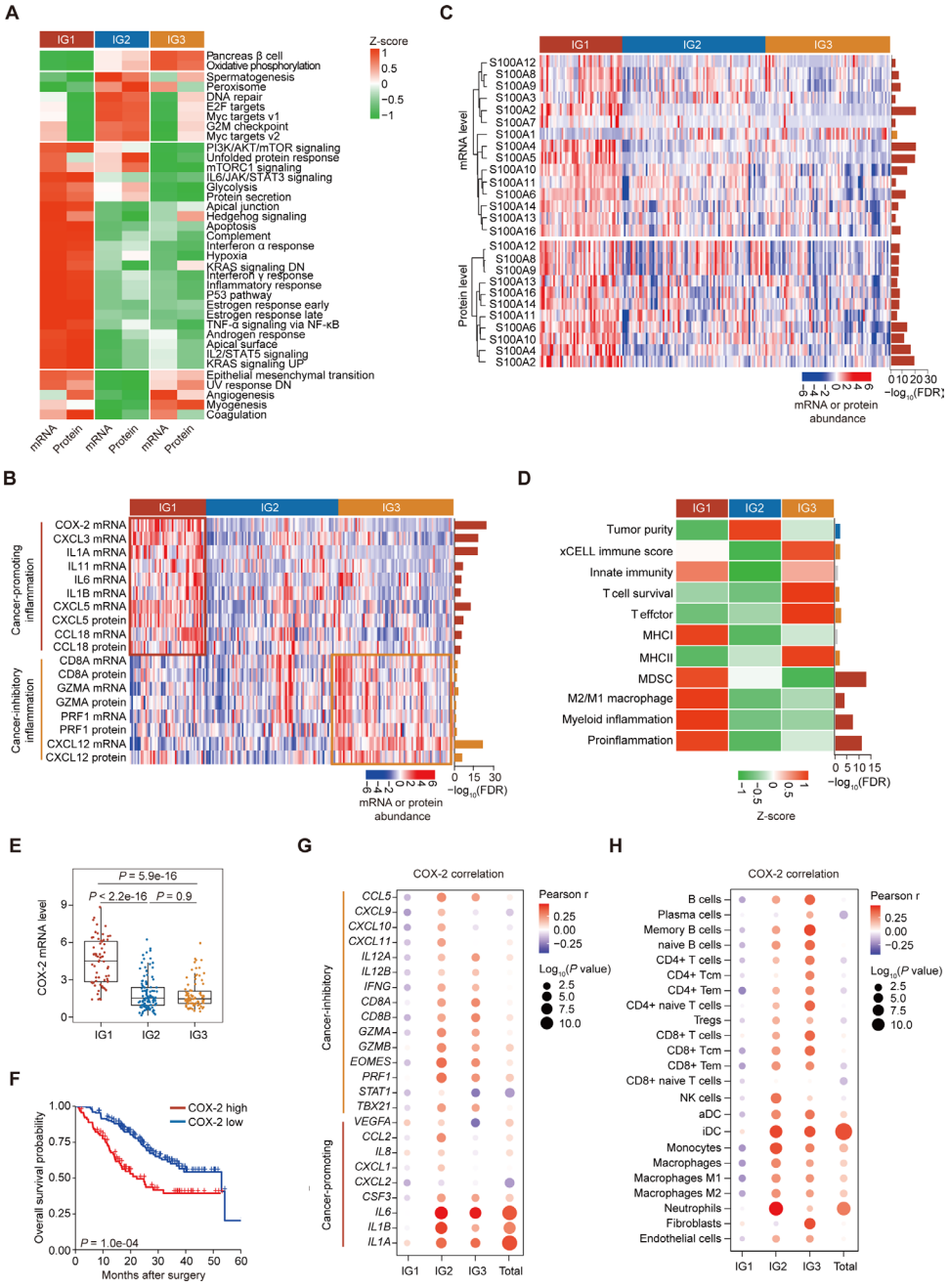

Figure 2 Distinct molecular features among the three immune subgroups. (A) Altered pathways at transcriptome and proteome levels among the three immune subgroups. (B) Heatmaps depicting mRNA and protein levels of various markers involved in cancer-promoting or cancer-inhibitory inflammation (adjusted analysis of variance (ANOVA)). (C) Heatmaps depicting mRNA and protein levels of S100A family members (adjusted ANOVA). (D) Signature scores among the three immune subgroups (adjusted ANOVA). (E) Comparisons of COX-2 mRNA levels among the three immune subgroups (Wilcoxon rank-sum test). (F) Kaplan-Meier curves for overall survival based on mRNA abundance of COX-2 (log-rank test). (G and H) Pearson correlation coefficient of COX-2 mRNA level with COX-2-associated inflammatory signature (COX-IS) genes (G) and the xCell enrichment scores of indicated cell subtypes (H).

supplemental figure S3F). Additionally, IG3 had the highest cytolytic score[29] and immunophenoscore[30] (online supplemental figure S3G,H), further supporting the hypothesis that IG3 could be more likely to respond to ICIs.

KRAS mutation-associated myeloid inflammation was dominant in IG1

We further investigated genomic alterations that could be associated with immunological features. IG2 had more frequent somatic copy number variations (SCNAs) (online supplemental figure S4A), in agreement with previous reports that SCNA burden negatively correlated with immune cell infiltration[31] (online supplemental figure S4B). When selecting subtype-specific mutated genes, we found that nearly half of tumors in IG1 were *KRAS* mutants (figure 3A,B and online supplemental table S3). *KRAS* mutation was negatively associated with

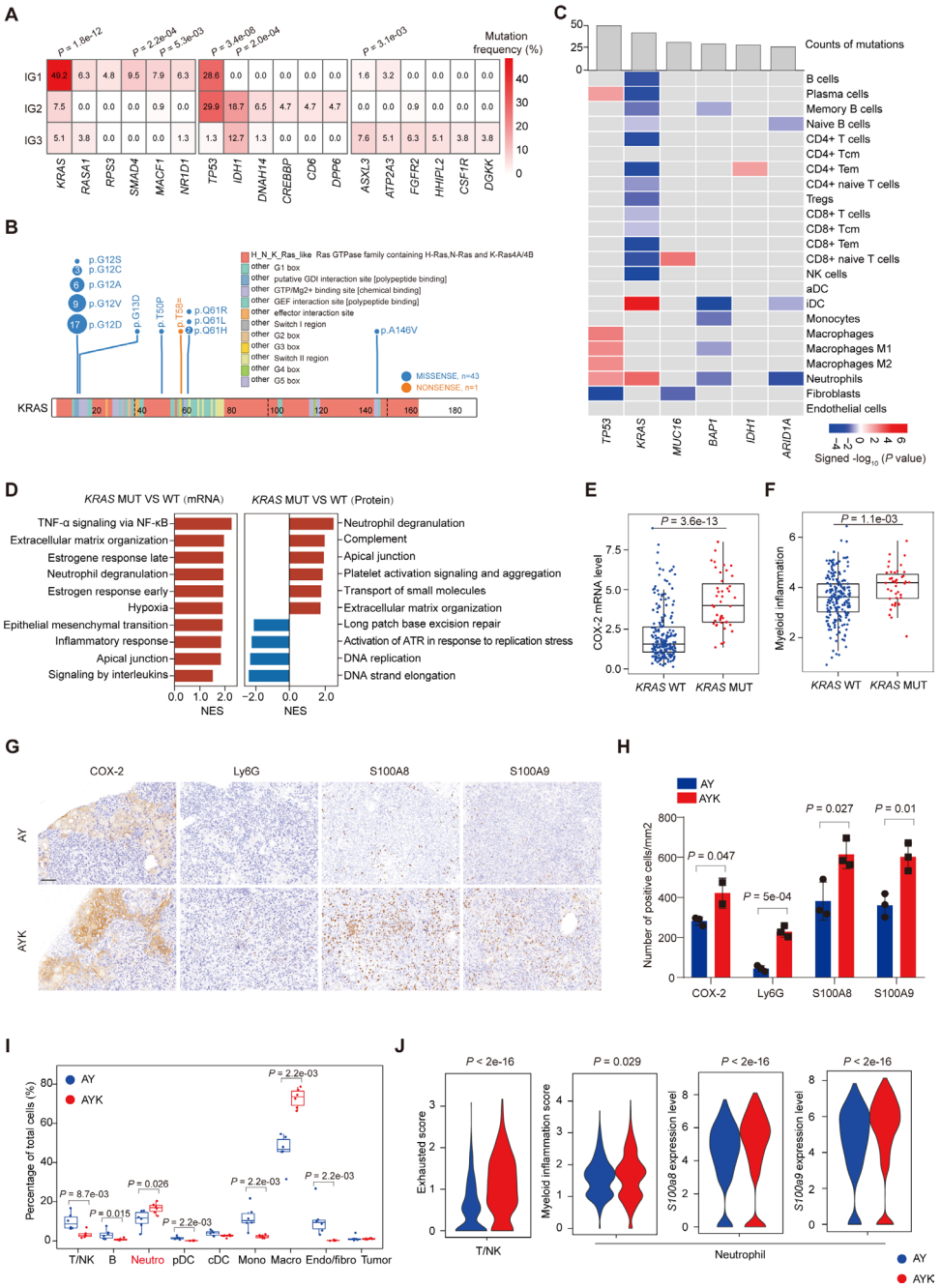

Figure 3 The association between *KRAS* mutation and myeloid inflammation. (A) Genes with significant differences in mutational frequency among the three immune subgroups (Fisher's exact test). (B) Somatic variants along KRAS protein in the Fudan University-intrahepatic cholangiocarcinoma (FU-iCCA) cohort. (C) Association between mutation profiles and immune/stromal signatures from xCell. Only significantly associations were shown (Wilcoxon rank-sum test). (D) Pathway enrichment analysis based on differentially expressed genes (left panel) and proteins (right panel) that associated with *KRAS* mutations. (E,F) COX-2 mRNA level (E) and myeloid inflammation score (F) in tumor samples with and without *KRAS* mutation (Wilcoxon rank-sum test). (G,H) Immunohistochemistry of COX-2, Ly6G, S100A8, and S100A9 (G) and quantification of their staining intensities (H). Representative data of triplicate experiments (mean±SEM). Scale bar, 100 µm. (I) Boxplot showing the fractions of indicated tumor microenvironment (TME) composition in AY (n=6) and AYK (n=6) tumors (analysis of variance (ANOVA)). (J) Violin plot showing the exhausted score in T/natural killer (NK) cells (left panel) and myeloid inflammation and *s100a8/s100a9* expression in neutrophils (right panel) in AY and AYK samples (ANOVA).

most xCell-derived adaptive immune and NK cell signatures, but positively correlated with iDC and neutrophil signatures (figure 3C and online supplemental table S3). GSEA at mRNA and protein levels both identified neutrophil degranulation to be the pathway most strongly associated with *KRAS* mutation (figure 3D and online supplemental table S3). Consistent with previous report,[32] *KRAS* mutation significantly and positively correlated with several inflammatory molecules, such as COX-2, IL-1A, IL-1B, IL-6, and S100A8/A9, resembling

the immunological feature of IG1 (figure 3E and online supplemental figure S4C). Tumors with *KRAS* mutation also displayed elevated myeloid inflammatory, COX-IS, and MDSC signatures, as well as decreased cytolytic signature (figure 3F, online supplemental figure 4D–F and online supplemental table S3). In Jusakul's cohort,[33] *KRAS* mutation also led to elevated neutrophil infiltration, COX-2/S100A8 expression, and neutrophil degranulation pathway (online supplemental figure S4G–J).

Considering that *PTGS2* was the most significantly upregulated gene associated with myeloid inflammation both in IG1 and *KRAS* mutant tumors, we hypothesized that *KRAS* mutation may upregulate COX-2 to produce PGE2, which promoted myeloid inflammation. Indeed, ectopic expression of $KRAS^{G12D}$ in iCCA cells significantly upregulated the mRNA and protein levels of COX-2 and COX-1, as well as increased PGE2 levels in the culture supernatant (online supplemental figure 4K–O). Transwell assay revealed that, compared with $KRAS^{WT}$, the culture supernatants from $KRAS^{G12D}$ significantly enhanced neutrophil migration (online supplemental figure S4P), which could be hampered by COX-2 inhibitor, celecoxib (online supplemental figure S4Q). $KRAS^{G12D}$ culture supernatant-treated neutrophils showed stronger immunosuppressive activity, as assessed by IL-2 production and apoptosis of preactivated Jurkat T cells (online supplemental figure S4R,S).

We next generated iCCA mouse models using oncogenic drivers myr-AKT and YAP^{S127A} in combination with $KRAS^{WT}$ (AY) or $KRAS^{G12D}$ (AYK) via the sleeping beauty system and hydrodynamic tail vein injection[34] (online supplemental figure S5A). Immunohistochemistry confirmed that AYK, but not AY tumors, were conspicuously infiltrated with neutrophils (positive for Ly6G, S100A8, and S100A9), while devoid of CD8+ T cells and B cells (figure 3G,H and online supplemental figure S5B,C). scRNA-seq analyses revealed that the proportions of neutrophil and macrophage were significantly higher in AYK tumors, whereas T/NK cells, B cell, and stromal cells were more abundant in AY tumors, consistent with multi-omics' results (figure 3I and online supplemental figure 5D–F). Neutrophils in AYK tumors showed higher myeloid inflammation and elevated expression of inflammatory markers like *S100a8*, *S100a9*, *Ptgs2*, and *Il1b*, accompanied by stronger exhausted phenotypes of T/NK cells (figure 3J and online supplemental figure S5G). Of note, *KRAS* mutation upregulated the expression of COX-2 both in tumor cells and the microenvironment (figure 3G,H and online supplemental figure S5G). Thus, excessive infiltration of neutrophils may account for *KRAS* mutation-associated myeloid inflammation. Overall, *KRAS* mutation had a critical role in subverting antitumor immunity to myeloid inflammation-associated immunosuppression (online supplemental figure S5H).

Antigen presentation defects are associated with immune exclusion in IG2

Defects in antigen presentation could interrupt neoantigen recognition and lead to tumor immune evasion, irrespective of tumor mutation burden (TMB). We thus explored the underlying roles of these avenues of immune evasion among the three immune subgroups (figure 4A). Despite relatively higher TMB and tumor neoantigen burden (TNB) in IG2, defects in antigen presentation through loss of heterozygosity in human leucocyte antigen (HLA LOH, p=2e-03) or alterations of the other components of antigen presentation machinery (APM, p=0.065) were frequently observed in IG2 (figure 4A,B; online supplemental figure S6A and online supplemental table S4). Such defects may hamper the cross-priming of naive T cells and subsequent tumor recognition by primed T cells, which may explain the reduction in T cell receptor/B cell receptor (TCR/BCR) diversity and RNA-seq reads mapping to VDJ loci in IG2 (online supplemental figure 6B–D).

We further calculated the immunoediting score for each tumor by quantifying the ratio of observed to expected numbers of predicted HLA class-I binding neoantigens, with a score of <1 indicating the presence of immunoediting.[35] Immunoediting scores decreased continuously from IG1 to IG3 (figure 4C and online supplemental table S4). Within each immune subgroup, only IG2 tumors with HLA LOH had a significantly higher immunoediting score, suggesting that tumor subclones in IG2 may be prone to HLA LOH-associated immune evasion (figure 4D). Overall, 15% (n=38) of patients exhibited HLA LOH, which had decreasing trends of overall survival (p=0.069, log-rank test) and recurrence-free survival (p=0.024, log-rank test) compared with the HLA intact patients (figure 4E,F).

The expression of immune checkpoints may reflect a cancer-adaptive immune response to an active immune system. We found a subgroup-specific pattern of these molecules, where IG2 had relatively few exclusively upregulated immune checkpoints (online supplemental figure S6E). HLA LOH correlated with some immune checkpoint molecules, such as programmed death ligand 1, and refined TMB as a biomarker of ICIs.[36] Comparing the multi-omics profiles between tumors with and without HLA LOH revealed differentially expressed mRNA and proteins that regulated metabolic reprogramming, cell-cycle transcriptional programs, and immune processes. HLA LOH was enriched with higher TMB/TNB, higher tumor purity, decreased interferon gamma pathway, and decreased major histocompatibility complex class I signatures. Likewise, T-cell survival and T-effector signatures were significantly reduced in tumors with HLA LOH (online supplemental figure S6F). Therefore, APM defects, especially HLA LOH, might involve in immune anergy and afterwards immune-exclusion despite the relatively high TMB in IG2 (figure 4G).

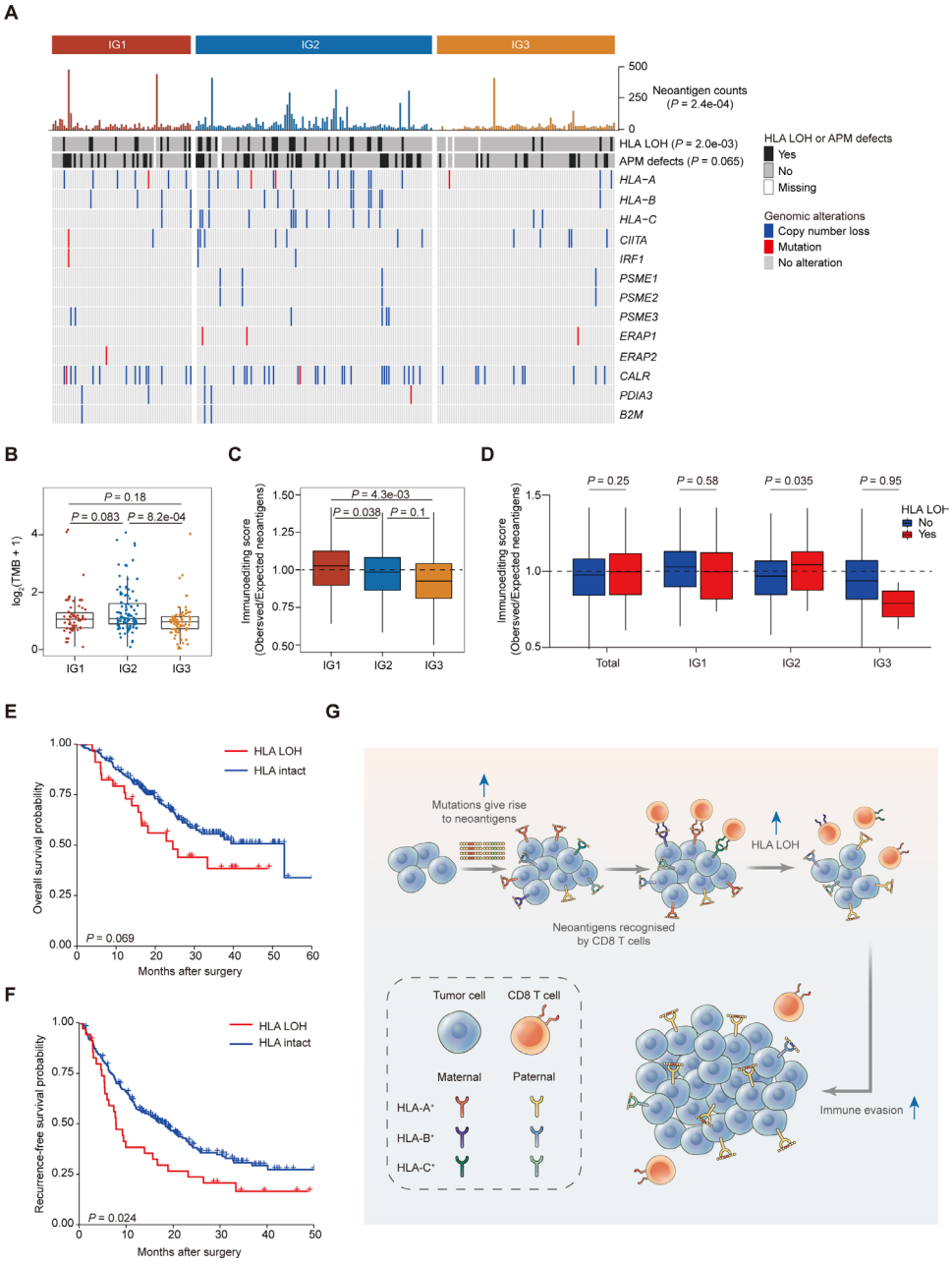

Figure 4 Antigen presentation defects occur frequently in IG2. (A) Antigen presentation machinery (APM) defects in each immune subgroup (Pearson's χ^2 test or Fisher's exact test). (B,C) Comparison of tumor mutation burden (TMB) (B) and immunoediting score (C) among the three immune subgroups (Wilcoxon rank-sum test). (D) Immunoediting score were plotted by HLA LOH status and immune classification (Wilcoxon rank-sum test). (E,F) Kaplan-Meier curves for overall survival (E) and recurrence-free survival (F) based on loss of heterozygosity in human leukocyte antigen (HLA LOH) status (log-rank test). (G) Model illustrating how HLA LOH may lead to immune escape in IG2.

Tertiary lymphoid structures are related to antitumor immunity in IG3

TLSs provide a pivotal microenvironment for generating antitumor immune responses. We used a previous TLS signature[37] to estimate TLS distribution and found that the mRNA levels of those genes, together with estimated TLS scores, were relatively upregulated in IG3 (figure 5A,B and online supplemental table S5). Pathological examination also confirmed that intratumoral TLSs were significantly accumulated in IG3 (figure 5C,D). Patients with both primary follicles (FL-I) and secondary follicles (FL-II) had higher estimated TLS scores compared with those with only Aggregates (Agg) and no TLSs (TLSs-), confirming the accuracy of TLS score (figure 5E and online supplemental figure S7A). Consistent with our latest report,[38] intratumoral TLSs predicted a better prognosis (figure 5F–H), and TLSs+ (Agg, FL-I, and FL-II) patients were characterized by early TNM stage (p=0.018), lack of microvascular invasion (p=0.033), absence of intrahepatic metastasis (p=0.011), and small tumor size (p=8.1e-04; online supplemental figure S7A and online supplemental table S5).

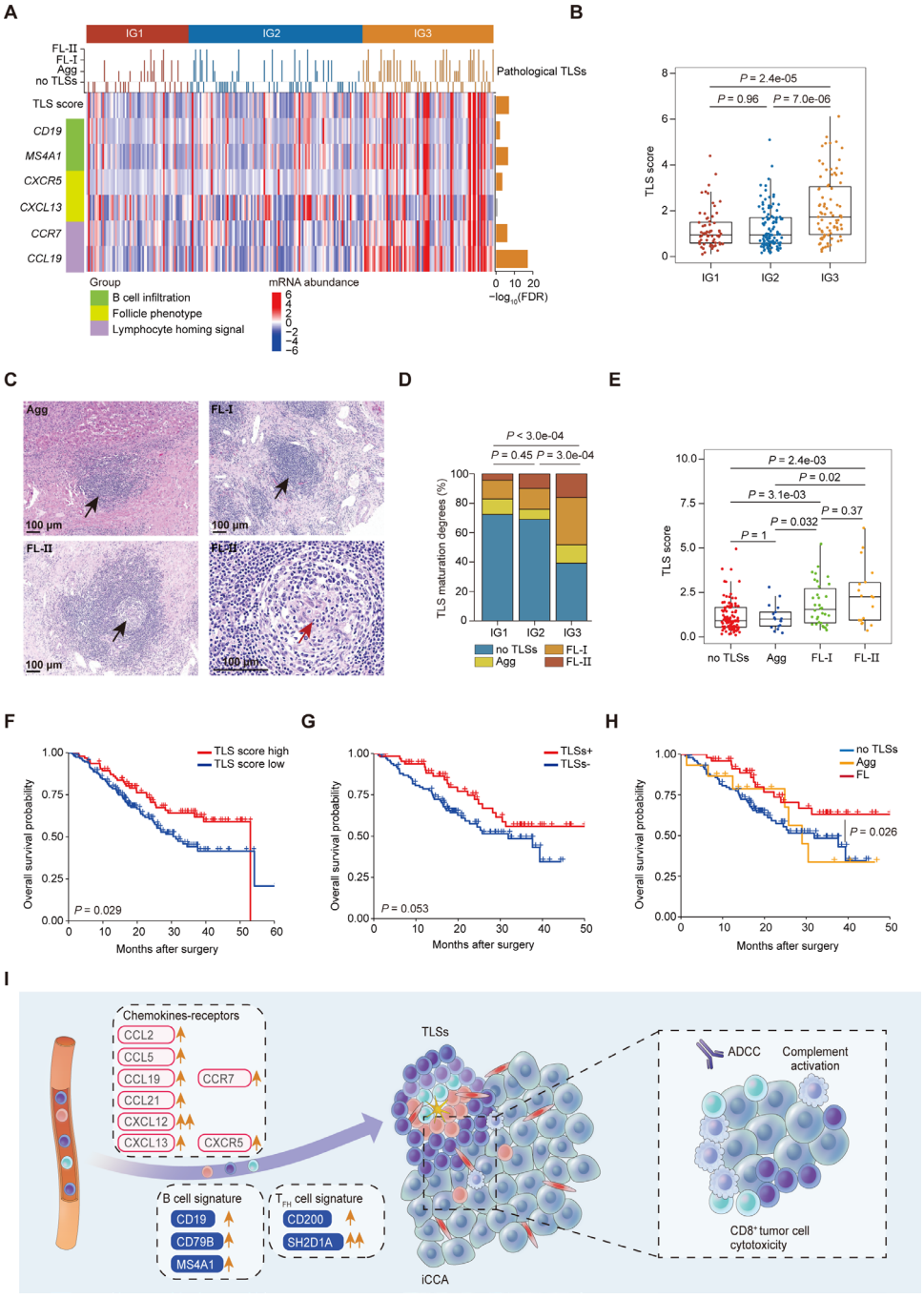

Figure 5 Tertiary lymphoid structures (TLSs) are enriched in IG3. (A) TLS-associated features in each immune subgroup (adjusted analysis of variance (ANOVA)). (B) Comparison of TLS scores among the three immune subgroups (Wilcoxon rank-sum test). (C) Histological appearance of intratumoral TLSs. (D) Comparison of H&E based intratumoral TLS maturation degrees among the three immune subgroups (Fisher's exact test). (E) Comparison of TLS scores among H&E-based intratumoral TLS maturation degrees (Wilcoxon rank-sum test). (F–H) Kaplan-Meier curves for overall survival based on TLS score (F), H&E-based intratumoral TLSs (G), and H&E based intratumoral TLS maturation degrees (H) (log-rank test). (I) Diagram showing the multi-omics profiles of regulators of TLS formation and function.

Multi-omics data indicated that TLSs+ tumors showed specific downregulation of pathways of G2M checkpoint, inflammatory response, and EMT, whereas upregulated ones in metabolism and peroxisome (online supplemental figure S7A). As expected, T cells and B cells, as well as coinhibitors, were enriched in TLSs+ tumors, suggesting an immune-activated phenotype (online supplemental figure S7B,C). Moreover, both cytolytic scores and COX-IS predicted a better response to immunotherapy for TLSs+ iCCA patients (online supplemental figure S7D,E). Thus, immunosurveillance in IG3 might be partially attributed to intratumoral TLSs (figure 5I), which predicted a better response to immunotherapy in this subgroup.

HBV infection is negatively associated with myeloid inflammation in iCCA

Hepatitis B virus (HBV) infection is the well-known risk factor for iCCA; however, little is known about the immunogenomic profile of HBV-related iCCA. We found that patients with HBV infection (n=68) were under-represented in IG1 (p=0.022), mutually exclusive with *KRAS* mutation (p=3.3e-03) and coexisted with *TP53* mutation (p=0.036) (figure 6A; online supplemental figure S8A and online supplemental table S6). HBV-positive tumors displayed an elevated cytolytic score, decreased myeloid inflammation signature and decreased COX-2 mRNA levels (figure 6B). Recent study proposed that ICIs showed efficacy for patients with HBV-positive hepatocellular carcinoma (HCC), rather than non-viral HCC.[39] Considering the negative impact of myeloid inflammation on immunotherapy,[40] the COX-IS score predicted worse responses to ICIs in HBV-negative subgroup (figure 6B). The transcriptome of patients with HBV-positive iCCA resembled the expression profile of other solid tumors that responded to ICIs[41] (figure 6C). Thus, the decreased myeloid inflammation observed in HBV-positive iCCA may define a population that could benefit from ICIs.

We additionally collected tumors and adjacent nontumor tissues from five HBV-positive and five HBV-negative iCCAs for scRNA-seq analyses (online supplemental figures S1A and S8B). Increased proportions of T/B/NK cells and reduced proportions of myeloid cells were observed in HBV-positive tumors (figure 6D), but HBV infection did not impact the proportions of each cluster in adjacent nontumor tissues (data not shown). We then classified the 10 patients into the closest immune subgroups according to the enriched gene sets (online supplemental figure S8C). At the CI of 0.7, four patients were excluded, with one (P06T), three (P03T/P09T/P10T), and two (P13T/P15T) samples grouping into IG1, IG2, and IG3, respectively. P06T, the only one remaining in IG1, was also the only patient with *KRAS* mutation among all the 10 iCCAs. The mRNA levels of inflammatory molecules, including COX-2, IL1A, S100A8, and S100A9, were higher in tumor or myeloid subsets in P06T (online supplemental figure S8D). The mRNA levels of cytolytic molecules, such as CD8A, GZMA, and PRF1, were downregulated in T cells in patient P06T, confirming the immunosuppressive TME in IG1 (online supplemental figure S8D).

Next, we performed unsupervised clustering of T/NK cells and myeloid cells. A total of 13 clusters emerged within T/NK cells (figure 6E and online supplemental figure S8E). The proportions of inflammatory CD4 T_CD154[42] were significantly higher in IG1, whereas the proportion of cytolytic NK_GNLY cluster slightly increased from IG1 to IG3 (online supplemental figure S8G). Both CD4_SOCS3[43] and NK_CD160[44] were enriched in HBV-positive tumors, implying that HBV infection alleviated inflammatory responses and enhanced cytolytic activities (figure 6F). The reclustering of myeloid lineage revealed 14 populations (figure 6G and online supplemental figure S8F). Notably, Macro_IL1B was the myeloid cluster with the most significant decrease in proportion after HBV infection, characterized by the exclusively high expression of *IL1A*, *IL1B*, *IL6*, and *TNF* (figure 6H and online supplemental figure S8F). COX-2 mRNA levels and the proinflammatory signatures were significantly higher in Macro_IL1B than the other myeloid clusters, demonstrating that Macro_IL1B was the primary source of myeloid inflammation (figure 6I). Indeed, myeloid cells from HBV-related iCCA showed downregulation of inflammatory pathways, such as complement and coagulation cascades and interferon alpha response (figure 6J). A smaller fraction of cycling cells was observed in HBV-positive than in HBV-negative samples, reflecting the relatively decreased proliferative capacities (figure 6H). Altogether, HBV-positive patients harbored a unique TME, with increased proportions of CD4_SOCS3 and NK_CD160 clusters, and reduced Macro_IL1B cluster and myeloid cell proliferation, which contributed to antitumor immunity.

Differentially expressed gene (DEG) analysis revealed that the top downregulated genes in macrophages of HBV-positive tumors included *CCL13*, *CTSC*, *FCGR2A*, *C1QA*, and *C1QB* (online supplemental figure S8H,I). NK cells in HBV-positive tumors upregulated several cytolytic-related genes, such as *KLRC2*, *GZMK*, and *CXCR6* (online supplemental figure S8J). In HBV-positive tumors, macrophages were characterized by downregulated inflammatory responses, whereas NK cells upregulated cytotoxicity and allograft rejection responses (figure 6K and online supplemental figure 8H–J). Collectively, HBV infection in iCCA may alleviate myeloid inflammation and promote antitumor immunity. Hence, HBV infection was slightly associated with longer overall survival in our cohort (p=0.091, log-rank test; figure 6L), consistent with a previous study.[45]

DISCUSSION

Tremendous sequencing studies have improved our understanding of the molecular pathogenesis of iCCA.[8–11 33] However, little is known about the immunogenomic profile of iCCA and how to leverage this information to maximize responses to immune therapies. Herein, we provided an immunogenomic characterization of iCCAs, involving WES, RNA-seq, proteomics, scRNA-seq and mouse model analyses that could enable the discovery of novel biological insights and identification of promising targets for precise oncological practice.

We identified three distinct immune subgroups with diverse clinical, immune, genetic, and molecular features. IG1 was defined by the enrichment of neutrophils and iDCs, as well as *KRAS* mutations. *KRAS* mutation is associated with the recruitment of myeloid cells and MDSCs into the TME, which then drives immune suppression.[46] Consistently, *KRAS* mutation may probably be the primary cause of myeloid inflammatory and immunosuppression

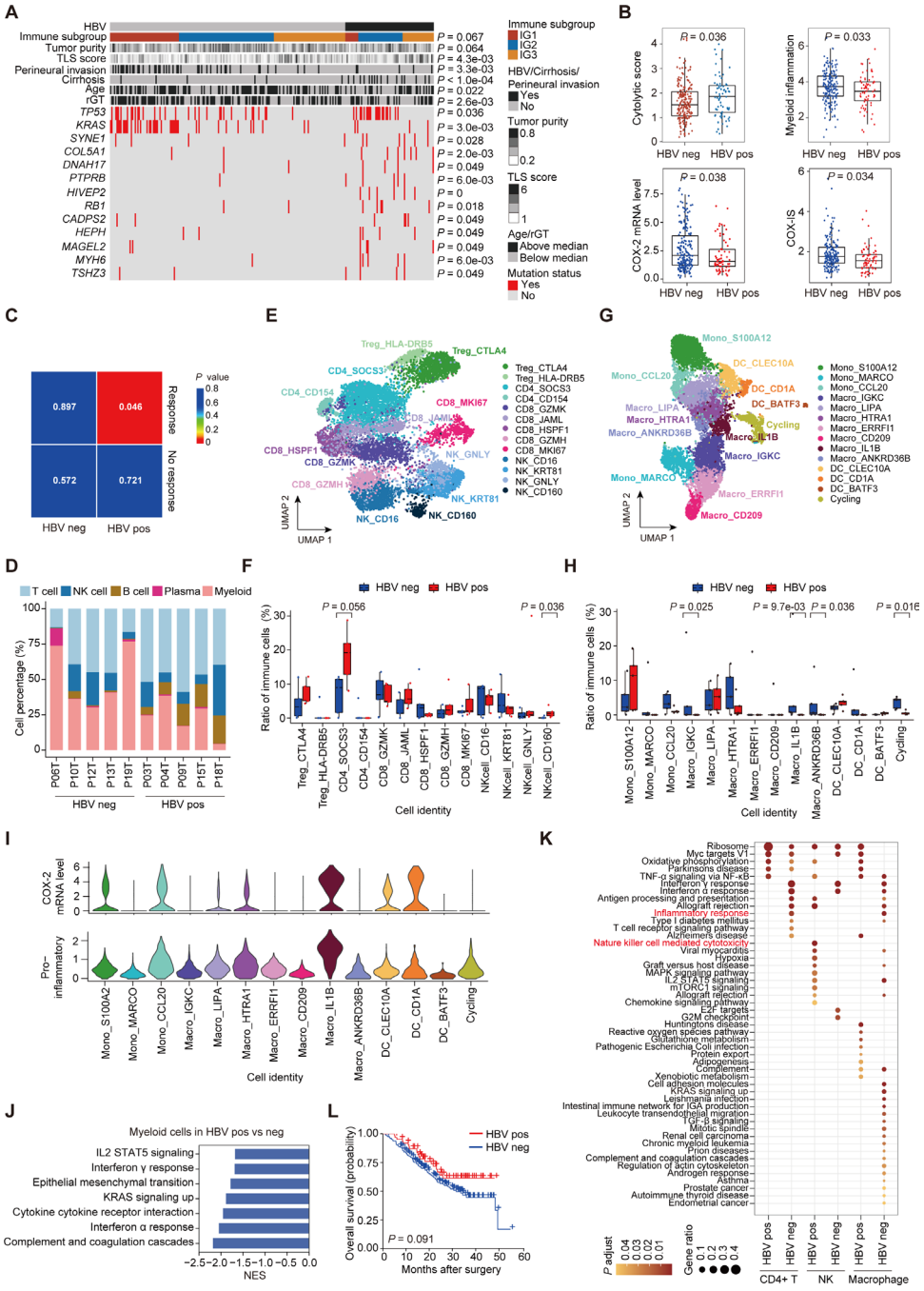

Figure 6 Influences of hepatitis B virus (HBV) infection on the immune microenvironment of intrahepatic cholangiocarcinoma (iCCA). (A) Associations of HBV infection with indicated features (analysis of variance (ANOVA), Pearson's χ^2 test, or Fisher's exact test). (B) Comparisons of representative signatures in patients with and without HBV infection (Wilcoxon rank-sum test). (C) Subclass mapping with other solid tumors treated with anti-PD-1 mAb (anti-programmed cell death protein 1 monoclonal antibody). (D) The proportion of indicated immune cells in tumor samples. (E) Uniform Manifold Approximation and Projection (UMAP) plot showing the subtypes of T/natural killer (NK) cells. (F) Boxplot showing the fractions of T/NK cells (ANOVA). (G) UMAP plot showing the subtypes of myeloid derived cells. (H) Boxplot showing the fractions of myeloid-derived cells (ANOVA). (I) Violin plot indicating the mRNA levels of COX-2 (upper panel) and proinflammatory scores (bottom panel) in myeloid subgroups. (J,K) Pathway enrichment analysis based on differentially expressed genes that associated with HBV infections in myeloid cells (J), CD4+ T cells, NK cells, and macrophages (K). (L) Kaplan-Meier curves of overall survival based on HBV infection status (log-rank test).

in IG1. IG2 was an immune-exclusion subgroup with high tumor purity, strong proliferative activity, and defects in APM. Some tumors in IG2 could potentially have an ancestral immune-active microenvironment, and then gradually became "exclusion" during the enrichment of HLA LOH (figure 4G). IG3 was dominated by adaptive immune cells, aDCs, and NK cells, demonstrating an immune-activated phenotype with the enrichment of

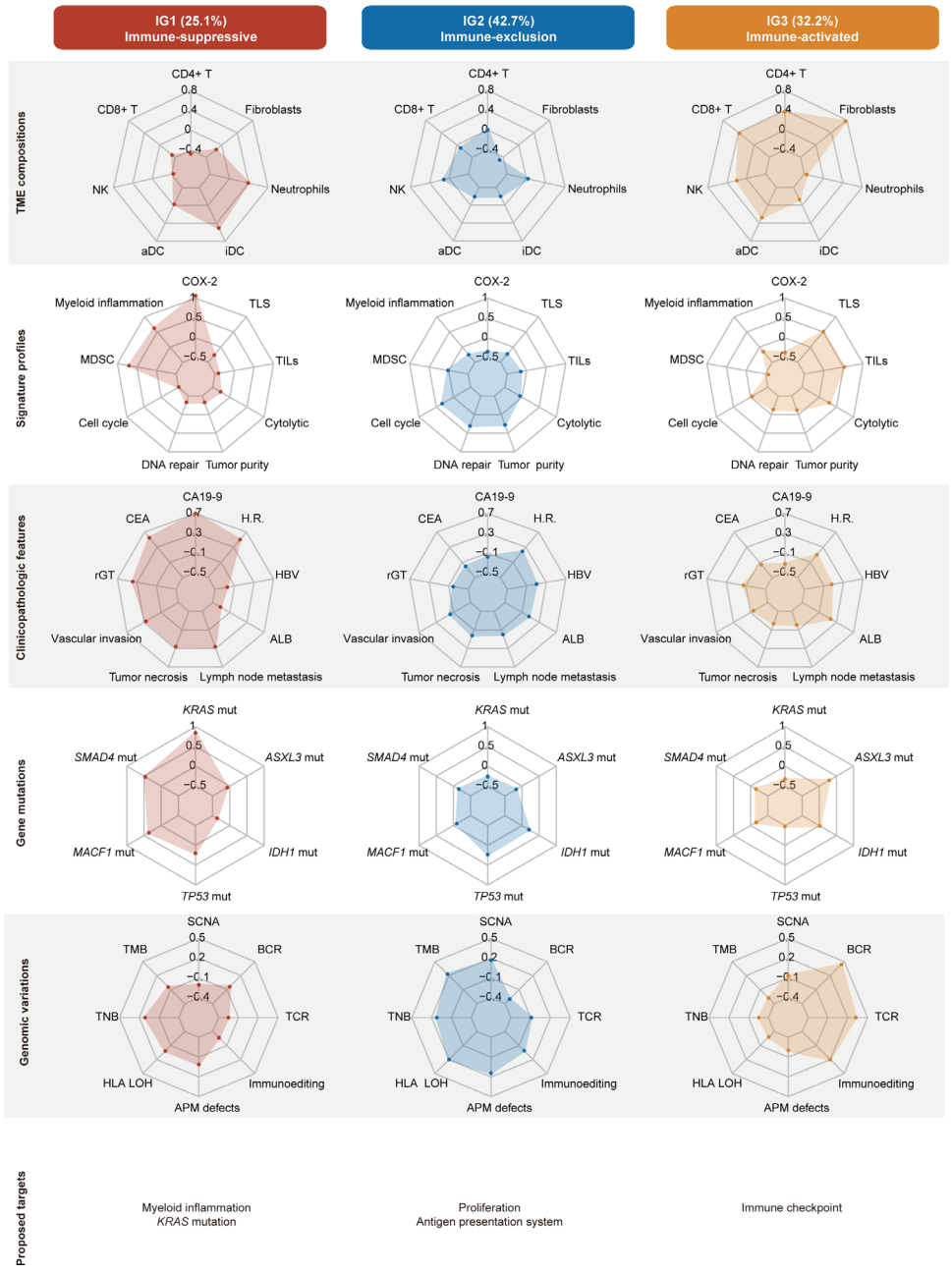

Figure 7 Summary of immunogenomic features of intrahepatic cholangiocarcinoma. Radar charts represented mean Z scores for the molecular features and clinical characteristics describing immune-suppressive, immune-exclusion, and immune-activated subgroups. Therapeutic targets of each subgroup were proposed.

TLSs. The immunogenomic features of the three immune subgroups were reproducible in multiple independent cohorts,[12 33] supporting that our classification was suitable and reliable.

Chronic inflammation induced by HBV infection increases the risk of HCC and iCCA. Using high-dimensional CyTOF analysis, Lim *et al*, revealed that HBV-related HCC microenvironment is more immunosuppressive and exhausted than that of non-viral-related HCC.[47] In contrast, we found that HBV infections alleviated myeloid inflammation and enhanced the cytolytic activity of NK cells in iCCA, indicating that this common etiology may lead to distinct microenvironments between HCC and iCCA. Recently, three randomized phase III clinical trials in more than 1600 patients with advanced HCC revealed that immunotherapy was superior in patients with viral-related HCC.[39] However, it is still unknown whether underlying viral hepatitis impacts on ICIs' response in iCCA. We here proposed that HBV infection in iCCA could counteract the excessive myeloid inflammation and potentially reinvigorate antitumor immunity, probably favoring the efficacy of ICIs. The reduced myeloid inflammation in patients with virus-related iCCA might be due to the selection for KRAS wild type tumors during persistent HBV infection.[48] Another rational explanation is the negative correlation between chronic

HBV infection and innate immune response, especially the function of neutrophils.[49]

Therapeutically, this study aimed to characterize iCCA immune subgroups amenable to specific individualized therapies (figure 7 and online supplemental table S7). IG1 might be responsive to myeloid targeted therapies, such as C-X-C motif chemokine receptor 2 (CXCR2) and colony stimulating factor receptor (CSFR) inhibitors to deplete or reprogram tumor-associated neutrophils and M2 macrophages, respectively. Recent success in selective inhibitors of *KRAS* G12C[50] may spark a renewed enthusiasm in targeting *KRAS* mutations in this immune-suppressive subgroup. IG2 may acquire better outcomes from specific CDK inhibitors, as well as strategies that regulate *HLA* and *APM* transcription. The enrichment of TLSs in IG3 and its potential role in the response to ICIs treatment may help guide clinical application of ICIs. Notably, the three immune subgroups showed distinct expression patterns of immune checkpoints, underscoring the need for personalized ICIs.

Our study had some limitations. The use of a retrospective cohort with varied clinicopathological features and treatments may require further prospective validation. In addition, immunostaining on TMAs for estimating immune cell infiltration was likely to over-represent or under-represent the density or distribution of each immune subset. In conclusion, our integrative multi-module analyses provide a comprehensive understanding of iCCA's immune landscape. The three immune subgroups with specific immune and non-immune profiles may have implications for the design of clinical trials using novel therapeutic strategies in iCCA.

Author affiliations
[1]Jinshan Hospital Center for Tumor Diagnosis & Therapy, Jinshan Hospital, Fudan University, Shanghai, China
[2]Shanghai Institute of Hematology, State Key Laboratory of Medical Genomics, National Research Center for Translational Medicine at Shanghai, Ruijin Hospital, Shanghai Jiao Tong University School of Medicine, Shanghai, China
[3]Department of Liver Surgery and Transplantation, Liver Cancer Institute, Zhongshan Hospital, Key Laboratory of Carcinogenesis and Cancer Invasion of Ministry of Education, Fudan University, Shanghai, China
[4]Key Laboratory of Computational Biology, Shanghai Institute of Nutrition and Health, University of Chinese Academy of Sciences, Shanghai, China
[5]Department of Gastroenterology & Hepatology, Ruijin Hospital, Shanghai Jiaotong University School of Medicine, Shanghai, China
[6]The Center for Microbes, Development and Health, Key Laboratory of Molecular Virology & Immunology, Institute Pasteur of Shanghai, University of Chinese Academy of Sciences, Shanghai, China
[7]Lester and Sue Smith Breast Center, Department of Molecular and Human Genetics, Baylor College of Medicine, One Baylor Plaza, Houston, TX 77030, USA
[8]Key Laboratory of Medical Epigenetics and Metabolism, Institutes of Biomedical Sciences, Fudan University, Shanghai, China
[9]Department of Analytical Chemistry and CAS Key Laboratory of Receptor Research, Shanghai Institute of Materia Medica, Chinese Academy of Sciences, Shanghai, China
[10]State Key Laboratory of Cell Biology, CAS Center for Excellence in Molecular Cell Science, Shanghai Institute of Biochemistry and Cell Biology, Chinese Academy of Sciences, Shanghai, China

Acknowledgements We thank Peng Cui, Bing Li, and Zhou Zhang (Burning Rock Biotech) for the assistance in bioinformatics analysis.

Contributors Conceptualization: QG, DG, and HZ; Methodology: JL, YD, BX, and QG; Formal analysis: JL, YD, BX, LD, XS, SJ, MW, and HF; Investigation: JL, GS, CS, MZ, XX, JM, and SZ; Resources: QG, DG, HZ, JF, JZ, BZ, XW, and XZ; Data curation: QG, YD, and JL; Writing: JL and QG; Visualization: YD and JL; Supervision, QG; Funding acquisition: QG and JL. QG is responsible for the overall content as guarantor.

Funding This work was supported by the National Natural Science Foundation of China (Grants 82130077, 81961128025, and 82103314), Research Projects from the Science and Technology Commission of Shanghai Municipality (Grants 20JC1418900 and 19XD1420700), Jinshan Hospital Flexible Mobile Talent Research Startup Fund (RXRC-2020-1), the Science and Technology Commission of Shanghai Municipality (20JC1418900), and China Postdoctoral Science Foundation (Grant 2020M681181).

Competing interests None declared.

Patient consent for publication Not required.

Ethics approval This study involves human participants and was approved by the Research Ethics Committee of Zhongshan Hospital, and written informed consent was obtained from each patient. Participants gave informed consent to participate in the study before taking part.

Provenance and peer review Not commissioned; externally peer reviewed.

Data availability statement Data are available in a public, open access repository. Data are available on reasonable request.

ORCID iDs
Jian Lin http://orcid.org/0000-0001-6457-7026
Hu Zhou http://orcid.org/0000-0001-7006-4737

REFERENCES

1 Sung H, Ferlay J, Siegel RL, *et al*. Global cancer statistics 2020: GLOBOCAN estimates of incidence and mortality worldwide for 36 cancers in 185 countries. *CA Cancer J Clin* 2021;71:209–49.
2 Lamarca A, Barriuso J, McNamara MG, *et al*. Molecular targeted therapies: Ready for "prime time" in biliary tract cancer. *J Hepatol* 2020;73:170–85.
3 Zhou Z, Wang P, Sun R, *et al*. Tumor-Associated neutrophils and macrophages interaction contributes to intrahepatic cholangiocarcinoma progression by activating STAT3. *J Immunother Cancer* 2021;9:e001946.
4 Shi G-M, Jian Z, Fan J, *et al*. Phase II study of lenvatinib in combination with GEMOX chemotherapy for advanced intrahepatic cholangiocarcinoma. *Journal of Clinical Oncology* 2021;39:e16163.
5 Imfinzi plus chemotherapy significantly improved overall survival in 1st-line advanced biliary tract cancer in TOPAZ-1 phase III trial at interim analysis, 2021. Available: https://www.astrazeneca.com/content/astraz/media-centre/press releases/2021/imfinzi-improved-survival-in-biliary-tract-cancer.html
6 Sia D, Jiao Y, Martinez-Quetglas I, *et al*. Identification of an Immune-specific class of hepatocellular carcinoma, based on molecular features. *Gastroenterology* 2017;153:812–26.
7 Diao P, Jiang Y, Li Y, *et al*. Immune landscape and subtypes in primary resectable oral squamous cell carcinoma: prognostic significance and predictive of therapeutic response. *J Immunother Cancer* 2021;9:e002434.
8 Andersen JB, Spee B, Blechacz BR, *et al*. Genomic and genetic characterization of cholangiocarcinoma identifies therapeutic targets for tyrosine kinase inhibitors. *Gastroenterology* 2012;142:1021–31.

9 Oishi N, Kumar MR, Roessler S, *et al*. Transcriptomic profiling reveals hepatic stem-like gene signatures and interplay of miR-200c and epithelial-mesenchymal transition in intrahepatic cholangiocarcinoma. *Hepatology* 2012;56:1792–803.
10 Sia D, Hoshida Y, Villanueva A, *et al*. Integrative molecular analysis of intrahepatic cholangiocarcinoma reveals 2 classes that have different outcomes. *Gastroenterology* 2013;144:829–40.
11 Dong L, Lu D, Chen R, *et al*. Proteogenomic characterization identifies clinically relevant subgroups of intrahepatic cholangiocarcinoma. *Cancer Cell* 2022;40:70–87.
12 Job S, Rapoud D, Dos Santos A, *et al*. Identification of four immune subtypes characterized by distinct composition and functions of tumor microenvironment in intrahepatic cholangiocarcinoma. *Hepatology* 2020;72:965–81.
13 Carapeto F, Bozorgui B, Shroff RT, *et al*. The immunogenomic landscape of resected intrahepatic cholangiocarcinoma. *Hepatology* 2022;75:297–308.
14 Aran D, Hu Z, Butte AJ. xCell: digitally portraying the tissue cellular heterogeneity landscape. *Genome Biol* 2017;18:220.
15 Carpino G, Cardinale V, Di Giamberardino A, *et al*. Thrombospondin 1 and 2 along with PEDF inhibit angiogenesis and promote lymphangiogenesis in intrahepatic cholangiocarcinoma. *J Hepatol* 2021;75:1377–86.
16 Liberzon A, Birger C, Thorvaldsdóttir H, *et al*. The molecular signatures database (MSigDB) hallmark gene set collection. *Cell Syst* 2015;1:417–25.
17 Taylor CT, Colgan SP. Regulation of immunity and inflammation by hypoxia in immunological niches. *Nat Rev Immunol* 2017;17:774–85.
18 Li W, Tanikawa T, Kryczek I, *et al*. Aerobic glycolysis controls myeloid-derived suppressor cells and tumor immunity via a specific CEBPB isoform in triple-negative breast cancer. *Cell Metab* 2018;28:87–103.
19 Aran D, Sirota M, Butte AJ. Systematic pan-cancer analysis of tumour purity. *Nat Commun* 2015;6:8971.
20 Hornburg M, Desbois M, Lu S, *et al*. Single-Cell dissection of cellular components and interactions shaping the tumor immune phenotypes in ovarian cancer. *Cancer Cell* 2021;39:928–44.
21 Wang S, Song R, Wang Z, *et al*. S100A8/A9 in inflammation. *Front Immunol* 2018;9:1298.
22 Xiao Y, Ma D, Zhao S, *et al*. Multi-Omics profiling reveals distinct microenvironment characterization and suggests immune escape mechanisms of triple-negative breast cancer. *Clin Cancer Res* 2019;25:5002–14.
23 Petitprez F, de Reyniès A, Keung EZ, *et al*. B cells are associated with survival and immunotherapy response in sarcoma. *Nature* 2020;577:556–60.
24 McDermott DF, Huseni MA, Atkins MB, *et al*. Clinical activity and molecular correlates of response to atezolizumab alone or in combination with bevacizumab versus sunitinib in renal cell carcinoma. *Nat Med* 2018;24:749–57.
25 Kawahara K, Hohjoh H, Inazumi T, *et al*. Prostaglandin E2-induced inflammation: relevance of prostaglandin E receptors. *Biochim Biophys Acta* 2015;1851:414–21.
26 Wang D, DuBois RN. Role of prostanoids in gastrointestinal cancer. *J Clin Invest* 2018;128:2732–42.
27 Dudek AM, Martin S, Garg AD, *et al*. Immature, semi-mature, and fully mature dendritic cells: toward a DC-Cancer cells interface that augments anticancer immunity. *Front Immunol* 2013;4:438.
28 Bonavita E, Bromley CP, Jonsson G, *et al*. Antagonistic inflammatory phenotypes dictate tumor fate and response to immune checkpoint blockade. *Immunity* 2020;53:1215–29.
29 Dufva O, Pölönen P, Brück O, *et al*. Immunogenomic landscape of hematological malignancies. *Cancer Cell* 2020;38:380–99.
30 Charoentong P, Finotello F, Angelova M, *et al*. Pan-Cancer Immunogenomic analyses reveal Genotype-Immunophenotype relationships and predictors of response to checkpoint blockade. *Cell Rep* 2017;18:248–62.
31 Davoli T, Uno H, Wooten EC, *et al*. Tumor aneuploidy correlates with markers of immune evasion and with reduced response to immunotherapy. *Science* 2017;355:eaaf8399.
32 Hamarsheh Shaima'a, Groß O, Brummer T, *et al*. Immune modulatory effects of oncogenic KRAS in cancer. *Nat Commun* 2020;11:5439.
33 Jusakul A, Cutcutache I, Yong CH, *et al*. Whole-Genome and epigenomic landscapes of etiologically distinct subtypes of cholangiocarcinoma. *Cancer Discov* 2017;7:1116–35.
34 Affo S, Nair A, Brundu F, *et al*. Promotion of cholangiocarcinoma growth by diverse cancer-associated fibroblast subpopulations. *Cancer Cell* 2021;39:866–82.
35 Rosenthal R, Cadieux EL, Salgado R, *et al*. Neoantigen-directed immune escape in lung cancer evolution. *Nature* 2019;567:479–85.
36 Montesion M, Murugesan K, Jin DX, *et al*. Somatic HLA class I loss is a widespread mechanism of immune evasion which refines the use of tumor mutational burden as a biomarker of checkpoint inhibitor response. *Cancer Discov* 2021;11:282–92.
37 Wang J, Jiang D, Zheng X. Tertiary lymphoid structure and CD8 T cell exclusion in minimally invasive adenocarcinoma. *medRxiv*2020.
38 Ding G-Y, Ma J-Q, Yun J-P, *et al*. Distribution and density of tertiary lymphoid structures predict clinical outcome in intrahepatic cholangiocarcinoma. *J Hepatol* 2022;76:608-618.
39 Pfister D, Núñez NG, Pinyol R, *et al*. Nash limits anti-tumour surveillance in immunotherapy-treated HCC. *Nature* 2021;592:450–6.
40 Nakamura K, Smyth MJ. Myeloid immunosuppression and immune checkpoints in the tumor microenvironment. *Cell Mol Immunol* 2020;17:1–12.
41 Montal R, Sia D, Montironi C, *et al*. Molecular classification and therapeutic targets in extrahepatic cholangiocarcinoma. *J Hepatol* 2020;73:315–27.
42 Shen X, Wang Y, Gao F, *et al*. Cd4 T cells promote tissue inflammation via CD40 signaling without de novo activation in a murine model of liver ischemia/reperfusion injury. *Hepatology* 2009;50:1537–46.
43 Ding F-M, Liao R-M, Chen Y-Q, *et al*. Upregulation of SOCS3 in lung CD4+ T cells in a mouse model of chronic PA lung infection and suppression of Th17-mediated neutrophil recruitment in exogenous SOCS3 transfer in vitro. *Mol Med Rep* 2017;16:778–86.
44 Sun H, Xu J, Huang Q, *et al*. Reduced CD160 expression contributes to impaired NK-cell function and poor clinical outcomes in patients with HCC. *Cancer Res* 2018;78:6581–93.
45 Jeong S, Tong Y, Sha M, *et al*. Hepatitis B virus-associated intrahepatic cholangiocarcinoma: a malignancy of distinctive characteristics between hepatocellular carcinoma and intrahepatic cholangiocarcinoma. *Oncotarget* 2017;8:17292–300.
46 Pylayeva-Gupta Y, Lee KE, Hajdu CH, *et al*. Oncogenic KRAS-induced GM-CSF production promotes the development of pancreatic neoplasia. *Cancer Cell* 2012;21:836–47.
47 Lim CJ, Lee YH, Pan L, *et al*. Multidimensional analyses reveal distinct immune microenvironment in hepatitis B virus-related hepatocellular carcinoma. *Gut* 2019;68:916–27.
48 Bose S, Sakhuja P, Bezawada L, *et al*. Hepatocellular carcinoma with persistent hepatitis B virus infection shows unusual downregulation of Ras expression and differential response to Ras mediated signaling. *J Gastroenterol Hepatol* 2011;26:135–44.
49 Hu S, Liu X, Gao Y, *et al*. Hepatitis B virus inhibits neutrophil extracellular trap release by modulating reactive oxygen species production and autophagy. *J Immunol* 2019;202:805–15.
50 Kim D, Xue JY, Lito P. Targeting KRAS(G12C): From Inhibitory Mechanism to Modulation of Antitumor Effects in Patients. *Cell* 2020;183:850–9.

Supplementary Materials and methods

Multimodule analysis

Bulk-tumor RNA-seq (n = 255) was utilized to stratify the FU-iCCA cohort. Then, WES (n = 249) and proteomics (n = 208) data elucidated the trans-omics connections and underlying molecular mechanisms. Meanwhile, H&E staining (n = 177), multiplex immunostaining (n = 188), and scRNA-seq (n = 10) were used to validate the immune features. The details of WES, RNA-seq, and proteomics analyses were conducted as described in our recent publication[1] and also briefly summarized as follows:

DNA Extraction and WES analysis

Genomic DNA was extracted from tumor and non-tumor liver tissues using QIAamp Fast DNA tissue kit (QIAGEN) according to manufacturer's protocol. DNA was quantified by the Qubit 3.0 (Invitrogen) and NanoDrop 2000 (Thermo Scientific). WES libraries were prepared and captured using the QuarPrep EZ DNA Library Kit and QuarHyb Reagent kit (DynastyGene Biotechnologies) following the manufacturer's instructions. The DNA library with 150 bp paired-end reads was sequenced with Illumina NovaSeq 6000 System. WES was conducted with a mean coverage depth of 205X (range: 90-300X) for tumor samples and 97X (range: 47-162X) for adjacent non-tumor liver samples. The exome sequencing data was first aligned to GRCh37/hg19 sequence reference using BWA MEM v 0.7.10 (http://bio-bwa.sourceforge.net/). After alignment, the GATK best practice workflow was applied on mapping results, including marking duplicates with picard v2.22.8

(https://broadinstitute.github.io/picard/) and base quality recalibration with GATK BaseRecalibrator v4.1.7.0 (https://gatk.broadinstitute.org/hc/en-us). Following the GATK guidance on tumor-normal matching samples, short somatic variants were called and filtered using GATK Mutect2 and other components. These variants were annotated using SnpEff v4.3T (https://pcingola.github.io/SnpEff/) and Annovar v2019-10-24 (https://doc-openbio.readthedocs.io/projects/annovar/en/latest/). variants filtering procedure, including the Catalogue Of Somatic Mutations In Cancer (COSMIC) (v91, 2020-04-07) (https://cancer.sanger.ac.uk/cosmic), the 1000 Genomes (v5b, 2015-08-24), NHLBI Exome Sequencing Project (ESP6500) (v2, 2014-12-22) (https://evs.gs.washington.edu/EVS/) and the Genome Aggregation Database (gnormAD) (v2.1.1 2019-04-09) (https://gnomad.broadinstitute.org/). To obtain high quality somatic variants, stringent downstream filters were used.

RNA Extraction and RNAseq analysis

Total RNA was extracted and purified from fresh frozen tissues using the Whole RNA extraction kit (TIAN GEN). RNA integrity was measured on an Agilent 2100 Bioanalyzer (Agilent Technologies). RNA with enough amount and good quality were used to prepare the transcriptome library. The cDNA synthesis, end-repair, A-base addition, and ligation of the Illumina index adapters were performed according to QuarPrep RNA Library Kit (DynastyGene Biotechnologies). Library quality was measured on an Agilent 2100 Bioanalyzer for product size and concentration. Paired-end libraries were sequenced by an Illumina NovaSeq 6000 System, with a sequence coverage of 139 million paired reads. RNA-seq data analysis identified 20,173 protein-coding genes with an average of 14,255 genes per sample, covering

the majority of the genes in proteomics. Sequence data were removed adaptors and low-quality reads using the Trimmomaticv 0.36. The cleaned sequence data were aligned to human reference genome (UCSC hg19 assembly) by STAR2(2.7.3a) in two-pass mode (with parameters: --chimSegmentMin 30 --chimJunctionOverhangMin 10 --alignSJDBoverhangMin 10 --alignIntronMax 200000 --alignSJstitchMismatchNmax 5 -1 5 5). The cleaned sequence reads were used for further qualification of gene expression. transcripts per million (TPM) values of each gene and transcript were calculated by Salmon with parameters of –seqBias --gcBias –posBias.

Proteomic Sample Preparation and Proteomic Analysis

Samples for MS were prospectively collected and 500 μL SDS lysis buffer was added into the powdered tissues for protein extraction, and sonicated at 20% amplitude for the total working time of 2 min with 5 s on and 5 s off (JY92-IIDN, Ningblio Scientz Biotechnology Co., LTD, China). The proteins were denatured at 95 ℃ for 5 min. Lysates were centrifuged at 12,000 g for 10 min to remove the insoluble debris and retain the supernatant for proteomic experiment. The tryptophan-based fluorescence quantification method was used to determine the protein concentration (Thakur et al., 2011). The equivalent of protein was digested by filter-aided sample preparation (FASP) procedure with 10 kDa centrifugal filter tubes (Millipore) and centrifuged at 12,000 g at 22 ℃. Concentration for eluted peptides was determined by BCA protein quantification kit. 400 μg peptides were dried by vacuum freeze-drying for the following experiment. The mixed samples proteins for the ‘internal reference’ were

also digested by FASP as well as the other protein samples. 41 μL x 2 anhydrous acetonitrile was added into two sets TMT reagents (0.8 mg) and mixed with 400 μg peptides (dissolved in 200 μL 100 mMTEAB) per channel. The samples were incubated for 1 hr at room temperature, and then quenched the labeling reaction by adding 16 μL 5% hydroxylamine into the samples and was incubated for 15 min at room temperature. The pooled samples of the labeled peptides in one set were dried by vacuum freeze-drying for the following desalting experiment through the C18 solid-phase extraction (3M Empore). 0.1% formic acid was used to resolve the peptides and 1 μg resolved peptides for proteomic analysis were separated on an Easy nLC 1000 UHPLC system (Thermo Fisher Scientific) with a 120 min LC gradient at 300 nL/min (Buffer A: 0.1% formic acid in water; Buffer B: 0.1% formic acid in acetonitrile) of a home-made 75 mm x200 mm diameter C18 column (ReproSil-Pur C18-AQ, 3.0 μm resin (Dr. Maisch GmbH, Germany)). The column was heated to 50°C using an in-house column heater and the gradient was set as 2%–5% B in 1 min; 5%–25% B in 94 min; 25%–40% B in 15 min; 40%–60% B in 3 min; 60%–100% B in 1 min; 100% B in 6 min. The spray voltage of the Q Exactive HF-X mass spectrometer was set at 1,800 V in positive ion mode and the ion transfer tube temperature was set at 320 °C. Xcalibur software was used for data-dependent acquisition. The 24 benchmark fractions were analyzed with a 90 min LC gradient and the gradient was set as 2%–5% B in 1 min; 5%–25% B in 67 min; 25%–40% B in 13 min; 40%–60% B in 3 min; 60%–100% in 1 min; 100% B in 5 min. The parameters of Q Exactive HF-X mass spectrometer were set the same as iCCA proteomic samples.

Download of TCGA data and calculation of immune scores

Updated FPKM gene expression data, clinical data and sample information in TCGA database were obtained from the Genomic Data Commons (https://portal.gdc.cancer.gov/) using the R package TCGAbiolinks[2]. Only primary solid tumor samples were enrolled in the analysis of immune score, which was calculated use R package ESTIMATE[3].

Microenvironment-related gene expression analysis and clustering

Gene expression data was log-transformed using $\log_2$ (FPKM+1). We first selected immune-cell-related markers of 21 immune cells and 2 stromal cells from the xCell database[4]. Then correlations between expression level of all genes and prognosis were calculated. For each gene, patients were separated into two subgroups by the mean value of the gene expression level, and the Cox proportional hazards regression model was used to calculated *P* value between subgroups and prognosis using R package survival. 4,782 prognosis-related genes were filtered with $P < 0.05$. After intersected with immune-cell-related markers, 170 genes were selected as pivotal microenvironment genes. Unsupervised hierarchical clustering method was used to classify 255 iCCA patients into different subgroups with clustering method 'ward.D2' and distance 'manhattan'. To identify the optimal cluster number, the ConsensusClusterPlus package and silhouette analysis in cluster package was used to assess clustering stability. Finally, three subgroups were identified (IG1, IG2, IG3).

Calculation of differentially expressed genes/proteins and functional enrichment analysis

The 170 pivotal microenvironment genes could be divided into two gene subgroups, IG1 enrichment and IG3 enrichment. We performed gene ontology (GO) enrichment analysis to identify the enrichment of functional pathways of two gene subgroups using the R package clusterProfiler. Differentially expressed genes and proteins between different conditions were calculated using R package limma. Genes with adjusted *P* value < 0.05 and fold change > 1.5 ($log_2FC > 0.58$) were set as significantly up-regulated, whereas with adjusted *P* value < 0.05 and fold change < 0.67 ($log_2FC < -0.58$) were set as significantly down-regulated. Proteins with adjusted *P* value < 0.05 and fold change > 1.25 ($log_2FC > 0.32$) were set as significantly up-regulated, whereas with adjusted *P* value < 0.05 and fold change < 0.8 ($log_2FC < -0.32$) were set as significantly down-regulated. Another functional enrichment analysis method, Gene Set Enrichment Analysis (GSEA), was also used to analysis differentially regulated pathways via R package clusterProfiler. Gene set enrolled in the GSEA analysis were download from the Molecular Signatures Database (MSigDB, v7.1) of the Broad Institute[5]. HALLMARK gene sets (H) and MSigDB curated gene sets of KEGG (C2), GO (C5), REACTOME (C2) were used to perform GSEA in a 1,000-gene-set with a two-sided permutation[6].

Calculation of immune-related and tumor-related scores

For the calculation enrichment score of different types of immune cells in each sample, we used single sample GSEA (ssGSEA) via GSVA package, with gene-sets of these immune cells downloaded from xCell database[4]. For the calculation of immune score (represents the infiltration of immune cells in tumor tissue) and stromal score (captures the presence of stroma in tumor tissue), R package ESTIMATE was used to predict the presence of infiltrating stromal/immune cells in tumor tissues using gene expression matrix[3]. The immunophenoscore of each patient was calculated using the algorithm and R script provided by Pornpimol Charoentong et al[7]. The mutation structure of KRAS were plotted using ProteinPaint.

Neoantigen predictions

Neoantigens were predicted by NetMHC (v4.0) and NetMHCpan (v4.1). The candidate neoantigens were filtered follow the criteria: 1) predicting as binders (IC50 < 500 nM in NetMHC or Score_EL > 0.1 in NetMHCpan). 2) neoantigen-derived genes are expressed in bulk RNA-seq data.

HLA genotyping and HLA-LOH prediction

POLYSOLVER was applied to investigate HLA gene genotypes. LOHHLA[8] was used to predict the LOH events for HLA genes based on the POLYSOLVER results. HLA LOH events were identified using the parameter $P < 0.001$. The coverage depth on HLA gene locations of tumor and normal samples of each patient were manually checked to verify the HLA LOH events.

Immunoediting analysis

We followed the method developed by Rooney et al.[9, 10] to analyze immunoediting in each patient. TCGA-HCC data was used as the driven null model. Referencing the published algorithm[8], 1,827 synonymous SNVs and 4,927 nonsynonymous SNVs were enrolled in the analysis. To estimate immunoediting, 3,390 mutational spectra were considered.

Somatic Copy Number Alteration (SCNA) analysis

For each patient, SCNAs were inferred by CNVkit[11] with default parameters and identified by Genomic Identification of Significant Targets in Cancer (GISTIC, version 2.0)[12]. The significantly gained or lost SCNA regions were determined by the default parameters in GISTIC and $\log_2$ ratio cut-off of ±0.8 was used to define SCNA amplification and deletion. The value of SCNA burden was calculated as the percentage of genes with amplification, gain, loss or deletion in each patient.

TCR and BCR analyses

Mapped RNA-sequencing reads were used to allelotype each patient by profiling TCR and BCR sequences with MiXCR as previously described[13].

Multiplexed immunostaining of Tissue MicroArray (TMA). The TMA of the FU-iCCA cohort was used to validate our immune subgroups. Multiplex staining of

CD1a (ab108309, Abcam), CD3 (ab135372, Abcam), CD8 (ab93278, Abcam), CD15 (ab135377, Abcam), CD66b (ab197678, Abcam), CD20 (ab78237, Abcam), CK19 (ab52625, Abcam), PDPN (ab236529, Abcam), and CD31(ab76533, Abcam) was performed by the Vectra Automated Quantitative Pathology Imaging and Analysis platform through multispectral imaging system and inFormTM image analysis software (PerkinElmer). Following the manufacturer's instruction (PerkinElmer, Opal® Kit), we scanned the whole field of each sample by using the PerkinElmer Vectra3® platform and quantified the results by using PerkinElmer Vectra3® platform as is described before[14]. All quantifications were evaluated blinded to patient clinical outcomes.

Pathological examination. The presence of intra-tumoral TLSs was assessed morphologically on H&E staining slides, using a previously published scale[15]. Briefly, TLSs were classified as: i) Aggregates (Agg): vague, ill-defined clusters of lymphocytes; ii) Primary follicles (FL-I): round-shaped clusters of lymphocytes without germinal center formation and iii) Secondary follicles (FL-II): follicles with germinal center formation. Cases were also further scored according to TLS maturation stages: i) Agg iCCA: tumors with only Agg and no FL-I or FL-II; ii) FL-I iCCA: tumors with at least FL-I, with or without Agg and without FL-II and iii) FL-II iCCA: tumors with at least 1 FLII regardless of the presence of Agg and FL-I.

Pathology TILs were estimated from H&E staining slides using international established guidelines, using a previously published scale[16]. Briefly, the relative

proportion of stromal area to tumor area was determined from the pathology slide of a given tumor region. TILs were reported for the stromal compartment (= per cent stromal TILs).

Mouse model construction

Six weeks old female FVB/N mice were ordered from Shanghai Branch of Beijing Vital River Laboratory Animal Technologies Co. Ltd. maintained under SPF housing with a maximum of five mice per cage. The experiments were performed following the institutional guidelines strictly and were approved by the Institutional Animal Care and Use Committee (IACUC) of the Shanghai Branch of Beijing Vital River Laboratory Animal Technologies Co. Ltd. (2017-0014). A sterile 0.9% NaCl solution/plasmid mix was prepared containing DNA. We prepared 20 μg of pT3-EF1α-HA-myr-Akt (Addgene, 31789), 30 μg of pT3-EF1a-YAP^{S127A} (Addgene, 86497), 10 μg of pT3-EF1a-KRAS^{WT} or 10 μg of pT3-EF1a-KRAS^{G12D}, and a 10:1 ratio of transposon to SB-luc transposase–encoding plasmid dissolved in 2 mL of 0.9% NaCl solution. Mice were injected with the solution into the lateral tail vein with a total volume corresponding to 10% of body weight in 6 to 8 seconds. Vectors for hydrodynamic delivery were produced using the QIAGEN plasmid PlusMega kit. Equivalent DNA concentration between different batches of DNA was confirmed to ensure reproducibility among experiments

Single cell RNA sequencing of mouse iCCA models

Tumors from AY (n = 6) and AYK (n = 6) iCCA mouse models were dissected using the Miltenyi Mouse Tumor Dissociation Kit and gentleMACS Octo-Dissociator (Miltenyi) following manufacturer's instructions. After filtering through a 70-mm filter, tumors were selected and droplet-based isolation of single cells was performed. Then, the cells were resuspended in 500 μL sample buffer and placed on ice and cell viability was tested using a BD Rhapsody Scanner instrument. Calcein AM (Invitrogen) and Drap7 (BD Biosciences) were added to the cell suspension to label the living and dead cells separately. Whole transcriptome libraries were prepared using the BD Rhapsody single-cell whole-transcriptome amplification workflow. Sequencing libraries were prepared using random priming PCR of the whole-transcriptome amplification products to enrich the 3′ end of the transcripts linked with the cell label and UMI. Sequencing libraries were quantified using a High Sensitivity DNA chip (Agilent) on a Bioanalyzer 2200 and the Qubit High Sensitivity DNA assay (Thermo Fisher Scientific). The library for each sample was sequenced by HiSeq X (Illumina, San Diego, CA) on a 150 bp paired-end run.

scRNA-seq data analyses for iCCA samples. For 10× Genomics scRNA-seq data analyses, raw reads were aligned to human reference genome (hg38, 2020-A) using Cell Ranger software (v6.0.0). The alignment reference and software were both provided by 10x Genomics (https://support.10xgenomics.com). The same software was used for unique molecular identifier (UMI) counting and filtration using default parameters. Raw count data were then analyzed with the R package Seurat (v4.0.0).

Cells that expressed less than 500 genes or over 20% mitochondrial RNA were filtered out. The expression matrix was merged and normalized using a global-scaling normalization method using Seurat. 2,000 variable genes were selected for dimensionality reduction. Principal component analysis (PCA) was performed on the variable genes and the resolution parameter to identify clusters was set to 0.8. Batch effects were corrected using ComBat. For visualization purposes, uniform manifold approximation and projection (UMAP) was performed. Clusters were identified using the top markers found in each cluster with an adjusted *P* value ≤ 0.05 and an average $\log_2$ fold change ≥ 0.1375. Markers to identify cell populations were selected from xCell database[4]. We also used another software SingleR to verify cell populations. In the analysis of gene expression similarity between bulk RNA-seq data and scRNA-seq data, we calculated the mean expression value of scRNA-seq samples. The ssGSEA algorithm was used to calculate the enrichment score of scRNA-seq samples and bulk RNA-seq samples using IG1 and IG3 enrich genes. Z-scores were calculated from the enrichment scores.

Functional experiments

Cell lines

HuCCT1, HCCC9810, HL60, and Jurkat cells are kept by Dr. Daming Gao's lab. These cell lines were cultured in RPMI.1640 medium supplemented with 10% FBS, 100 units of penicillin and 100 mg/mL streptomycin.

Plasmids and lentivirus-mediated construction of stable cell lines

The Myc-tagged coding sequence of human *KRAS* and *KRAS G12D* was cloned into the lentiviral vector pLEX-MCS-CMV-puro (Thermo Scientific Open Biosystems) to generate corresponding expression plasmids. pLEX-MCS-CMV-puro lentiviral packaging and generation of HuCCT1 ($KRAS^{G12D}$ iCCA cell line) and HCCC9810 ($KRAS^{WT}$ iCCA cell line) stable cell lines by infection were performed according to the protocol before[17].

Real-time quantitative PCR (qRT-PCR)

Total RNA was extracted from cells using TRIzol Reagent (Invitrogen, Thermo Fisher Scientific) according to the manufacturer's instructions. Total RNA was reverse transcribed into first-strand cDNA using the ABScript II RT Master Mix for qPCR Kit (ABclonal). The cDNAs were then used for real-time PCR (qPCR) on a CFX96 Touch Real-Time quantitative PCR System (Bio-Rad) using TB Green Premix® Ex Taq II (Tli RNaseH Plus; Takara). Human *GAPDH* was served as the internal control. The relative quantification of gene expression was analyzed by using the $2^{-\Delta\Delta Ct}$ method.

Western blot analysis

Cells were lysed in EBC lysis buffer (50 mM Tris HCl, pH 8.0, 120 mM NaCl, 0.5% Nonidet P-40) supplemented with protease inhibitors (Selleck Chemicals) and phosphatase inhibitors (Selleck Chemicals). 30 μg total proteins were separated by 10% SDS-PAGE gel and blotted with indicated primary antibodies. Primary antibodies used for western blot analysis were as follows: Myc (2276s, Cell Signaling Technology), COX-1 (9896s, Cell Signaling Technology), COX-2 (12282s, Cell

Signaling Technology), β-actin (4970s, Cell Signaling Technology). All western blot gel images were obtained with an Minichemi 610 chemiluminescent imager (Sagecreation, Beijing, China).

Elisa

The protein levels of PGE2 and IL-2 in culture medium were quantified by enzyme-linked immunosorbent assay (ELISA) kits (KGE004B, R&D Systems and 70-EK102-48, MultiSciences). Cell-free supernatants were collected and tested according to manufacturer's protocols. Absorbance at 450 nm was measured using a microplate reader.

Transwell assay

Neutrophil model derived from the differentiation of HL60 (dHL60) cells after 120 h culture in RPIM1640 medium supplemented with 10% FBS and 1.25% dimethyl sulfoxide (DMSO). The supernatant of HuCCT1/HCCC9810 and the complete culture medium were used to prepare the conditional culture medium at the ratio of 3:1. For the neutrophil migration assay, 1×10^5/200 μl neutrophils (from induced HL60 cells) were added to each upper chamber (5 μm, LABSELECT, 14331). The lower chambers contained conditioned medium from HuCCT1/HCCC9810 cells (incubated for 12 h). The number of neutrophils migrating from the upper chamber was counted microscopically.

Apoptosis detection

Jurkat T cells were pre-activated with human CD3/CD28 T cell Activator (STEMCELL, 10971) for 24 h. At the same time, dHL60 cells were treated with

indicated culture supernatants from HuCCT1 and HCCC9810. Then, the activated Jurkat T cells were cocultured with culture supernatants-treated dHL60 cells at the ratio of 1:1 for 24 hours. Cells were suspended in FACS buffer containing 1% FBS and 0.1% NaN3 and CD3+ Jurkat T cells were gated for further apoptosis analysis. The data were collected on an LSR-Fortessa X20 Flow Cytometer (BD Biosciences). The annexin V/PI apoptosis flow kit was purchased from BD Biosciences (559763).

Immunohistochemistry (IHC)

Tumor issues from mouse models were collected and fixed in 10% formalin overnight and embedded in paraffin. FFPE sections were prepared for staining using standard protocols for xylene and alcohol gradient for deparaffination. Antigen retrieval was performed in the pressure cooker (95℃ for 30 min) to remove aldehyde links formed during initial fixation of tissues. Slides were incubated with primary antibodies, including anti-COX-2 (Cell Signaling Technology, 12282s), anti-Ly6G (Abcam, ab238132), anti-S100A8 (Proteintech, 15792-1-AP), anti-S100A9 (Proteintech, 14226-1-AP), anti-CD8 (Abcam, ab217344) and anti-CD19 (Abcam, ab245235). Sections were incubated and then developed with Dako REAL™ EnVision™ Detection System (DAKO, K5007). The whole IHC slide was scanned and quantified with automated acquisition system (TissueFAXS Plus, TissueGnostics GmbH, Austria).

Statistical analysis and visualization. All of the statistical analyses were performed with R software (version 4.0.2, http://www.R-project.org). Student's t-Test and Wilcoxon rank sum test were utilized to compare continuous and categorical variables

between two subgroups or conditions, such as immune-related score, functional-related score, clinical features and SCNA levels in each subgroup. For multi-group comparison, we used ANOVA to estimate the *P* value. Correlation matrices of immune cells were calculated using Pearson correlation and visualized using R package corrplot. Correlation plots between two features such as immune score and stromal score were also calculated using Pearson correlation. Survival curves were estimated with the Kaplan-Meier method and compared using a log-rank test. The Kaplan-Meier survival curves were plotted by R ggsurvplot package. Variables associated with overall survival were identified using univariate Cox proportional hazards regression models. Significant factors in univariate analysis were further subjected to a multivariate Cox regression analysis in a forward LR manner. The FDR correction was utilized in multiple tests to decrease false positive rates. R package ggplot2 and pheatmap were used for visualization. For functional experiments, each was repeated at least three times independently, and results were expressed as mean ± standard error of the mean (SEM). Statistical analysis was performed using GraphPad Prism (version 8).

References

1. Dong L, Lu D, Chen R, et al. Proteogenomic characterization identifies clinically relevant subgroups of intrahepatic cholangiocarcinoma. *Cancer Cell* 2021.
2. Colaprico A, Silva TC, Olsen C, et al. TCGAbiolinks: an R/Bioconductor package for integrative analysis of TCGA data. *Nucleic Acids Res* 2016;44:e71.
3. Yoshihara K, Shahmoradgoli M, Martinez E, et al. Inferring tumour purity and stromal

and immune cell admixture from expression data. *Nat Commun* 2013;4:2612.

4. Aran D, Hu Z, Butte AJ. xCell: digitally portraying the tissue cellular heterogeneity landscape. *Genome Biol* 2017;18:220.
5. Liberzon A, Birger C, Thorvaldsdottir H, et al. The Molecular Signatures Database (MSigDB) hallmark gene set collection. *Cell Syst* 2015;1:417-425.
6. Subramanian A, Tamayo P, Mootha VK, et al. Gene set enrichment analysis: a knowledge-based approach for interpreting genome-wide expression profiles. *Proc Natl Acad Sci U S A* 2005;102:15545-50.
7. Charoentong P, Finotello F, Angelova M, et al. Pan-cancer Immunogenomic Analyses Reveal Genotype-Immunophenotype Relationships and Predictors of Response to Checkpoint Blockade. *Cell Rep* 2017;18:248-262.
8. McGranahan N, Rosenthal R, Hiley CT, et al. Allele-Specific HLA Loss and Immune Escape in Lung Cancer Evolution. *Cell* 2017;171:1259-1271 e11.
9. Newman AM, Liu CL, Green MR, et al. Robust enumeration of cell subsets from tissue expression profiles. *Nat Methods* 2015;12:453-7.
10. Rooney MS, Shukla SA, Wu CJ, et al. Molecular and genetic properties of tumors associated with local immune cytolytic activity. *Cell* 2015;160:48-61.
11. Talevich E, Shain AH, Botton T, et al. CNVkit: Genome-Wide Copy Number Detection and Visualization from Targeted DNA Sequencing. *PLoS Comput Biol* 2016;12:e1004873.
12. Mermel CH, Schumacher SE, Hill B, et al. GISTIC2.0 facilitates sensitive and confident localization of the targets of focal somatic copy-number alteration in human

cancers. *Genome Biol* 2011;12:R41.

13. Losic B, Craig AJ, Villacorta-Martin C, et al. Intratumoral heterogeneity and clonal evolution in liver cancer. *Nat Commun* 2020;11:291.

14. Ma J, Zheng B, Goswami S, et al. PD1(Hi) CD8(+) T cells correlate with exhausted signature and poor clinical outcome in hepatocellular carcinoma. *J Immunother Cancer* 2019;7:331.

15. Calderaro J, Petitprez F, Becht E, et al. Intra-tumoral tertiary lymphoid structures are associated with a low risk of early recurrence of hepatocellular carcinoma. *J Hepatol* 2019;70:58-65.

16. Rosenthal R, Cadieux EL, Salgado R, et al. Neoantigen-directed immune escape in lung cancer evolution. *Nature* 2019;567:479-485.

17. Gao Q, Zhu H, Dong L, et al. Integrated Proteogenomic Characterization of HBV-Related Hepatocellular Carcinoma. *Cell* 2019;179:561-577 e22.

Supplementary Figure legends

Figure S1 Workflow and consensus clustering of multi-omics data of the FU-iCCA cohort. (A) Workflow of the iCCA multi-omics study. iCCA tumor samples from a consecutive cohort of patients were obtained for WES (n = 249), RNA-seq (n = 255), proteomics (n = 208), H&E (n = 177), multiplex immunostaining (n = 188), and scRNA-seq (n = 10) analyses. (B) ESTIMATE immune scores from our cohort and other TCGA cancer types. (C) The procedure for constructing compendium of microenvironmental cells and clustering. (D,E) Consensus cumulative distribution function (CDF) plot (D) and delta area (change in CDF area) plot (E) of 170 prognostic gene-based classification were shown. (F) Correlations between mRNA and protein abundance in 103 mRNA-protein pairs from 170 prognostic microenvironment genes. (G) Unsupervised hierarchical clustering of the FU-iCCA cohort based on the 103 proteins identified three subgroups. (H) Relative abundance and proportion of samples harboring the indicated clinical covariate in the given immune subgroup (Wilcoxon rank sum test, Pearson's chi-square test, or Fisher's exact test). (I) Representative multiplex immunostaining images to show the distribution of PDPN+ lymphatic vessels and CD31+ blood vessels among the three immune subgroups (left panel). Quantification of staining intensities for the indicated markers are shown (ANOVA, right panel). (J) Representative H&E images from the FU-iCCA cohort were shown to display the indicated pathological TIL estimates. (K) Box plot showing the pathological TILs among three immune subgroups (ANOVA). (L) Representative multiplex immunostaining images to show the distribution of

CD66b+ neutrophils among the three immune subgroups (left panel). Quantification of staining intensities for the indicated markers are shown (right panel). Green arrows: CK19-CD66b+ (ANOVA).

Figure S2 Validations of our grouping strategy in external cohorts. (A,B) Heatmap with indicated immunogenomic features (A, left panel), Kaplan–Meier curves (A, right panel) and multivariate Cox proportional hazards model (B) for overall survival based on our subgrouping standard in Jusakul et al.'s cohort. H.R., Hazard ratio. C.I., confidence interval. (C,D) Heatmap with indicated immunogenomic features (C, left panel) and Kaplan–Meier curves (C, right panel) and multivariate Cox proportional hazards model (D) for overall survival based on our subgrouping standard in Job et al.'s cohort. H.R., Hazard ratio. C.I., confidence interval. (E-H) Comparisons of immune subgroups to the subgroups resulted from previously reported standards (E) and the heatmap of clustering analysis of Anderson et al (F), Oiishi et al (G), and Job et al (H). The *P* values were calculated by Pearson's Chi-square-test.

Figure S3 Potential different immunogenomic features of the three immune subgroups. (A) Principal-component feature loadings (magnitude and direction) shown in the variables factor map. Vectors were colored according to a major biological classification of cancer hallmark gene sets and ESTIMATE tumor purity. (B,C) The means of loadings per hallmark gene set for PC1 (B) and PC2 (C),

respectively. The *P* values were calculated by Wilcoxon rank sum test. (D) Hierarchically-clustered heatmap of normalized enrichment scores (NES). Rows indicated hallmark gene sets and columns indicated tumor samples. Normalized tumor purity values and immune subgroups shown on top. (E) Hallmark pathway enrichment analysis after controlling for tumor purity (adjusted ANOVA). (F-H) Comparisons of COX-IS (F), cytolytic score (G), and immunophenoscore (H) among the three immune subgroups (Wilcoxon rank sum test).

Figure S4 Association of the immune subgroups with genomic alterations. (A) Comparison of total SCNA levels among the three immune subgroups (Wilcoxon rank sum test). (B) Correlation analysis between ESTIMATE immune score and SCNA burden. (C) The expression heatmaps depicted mRNA and protein levels of various markers involved in cancer-promoting or cancer-inhibitory inflammation (Wilcoxon rank sum test). (D,E) Comparisons of COX-IS (D) and cytolytic score (E) in tumor samples with and without *KRAS* mutation (Wilcoxon rank sum test). (F) GSEA analysis based on the MDSC signature up gene set in tumor samples with and without *KRAS* mutation. (G-I) Comparisons of neutrophil infiltration (G), COX-2 mRNA level (H), and S100A8 mRNA level (I) of patients with and without *KRAS* mutations in Jusakul's cohort (Wilcoxon rank sum test). (J) Pathway enrichment analysis based on differentially expressed genes that associated with *KRAS* mutations in Jusakul's cohort (Wilcoxon rank sum test). (K-O) HuCCT1 and HCCC9810 cells ectopically expressing Myc-tag $KRAS^{WT}$ or Myc-tag $KRAS^{G12D}$ were generated and then

qRT-PCR (K,L), western blot (M), and ELISA (O) were performed to detect the indicated molecules. Quantification of three independent western blotting assays were shown (N). The NC group indicated cell lines without transfection. Representative data of triplicate experiments were shown. Data are expressed as mean ± SEM (ANOVA). nd, not determined. (P) Transwell assay showing that the culture supernatants from $KRAS^{WT}$ and $KRAS^{G12D}$ overexpressing HuCCT1 and HCCC9810 significantly enhanced the migration of dHL60. Representative data of triplicate experiments were shown. Data are expressed as mean ± SEM (ANOVA). (Q) Culture supernatants from $KRAS^{G12D}$ overexpressing HuCCT1 and HCCC9810 treated with DMSO or 15 μM COX-2 inhibitor Celecoxib for 48 h were collected. Then the DMSO treated supernatant (DMSO group), DMSO treated supernatant plus 15 μM Celecoxib (CELE untreated group), and Celecoxib treated supernatant (CELE treated group) were used to perform the transwell assay. Representative data of triplicate experiments were shown. Data are expressed as mean ± SEM (ANOVA). (R,S) The effects of pre-treatment dHL60 by indicated culture supernatants on anti-CD3/CD28 activated Jurkat T cells. The apoptosis (R) and IL-2 (S) secretion of Jurkat T cells were detected. Representative data of triplicate experiments were shown. Data are expressed as mean ± SEM (ANOVA).

Figure S5 The *KRAS* mutation-associated tumor microenvironment of mouse iCCA model. (A) Schematic of vectors used in the hydrodynamic injections. Luc, luciferase. (B,C) Immunohistochemical analysis for CD8 and CD19 (B) and

quantification of staining intensities for the indicated markers are shown (C). Representative data of triplicate experiments were shown. Data are expressed as mean ± SEM. (D) UMAP plot showing the annotation and color codes for cell types in the FU-iCCA ecosystem. (E) Violin plot showing the expression of marker genes in the indicated cell types. The top dots label the clusters corresponding to specific cell types in (D) and the bottom shows indicated marker genes. (F) UMAP plot showing the group origin in AY and AYK mouse iCCA samples. (G) Violin plots showing *Ptgs2* and *Il1b* expression of indicated cell composition in AY and AYK samples, respectively. The *P* values were calculated by ANOVA. (H) Overview of *KRAS* mutation-dominated myeloid inflammation.

Figure S6 Immunogenomic features of IG2. (A) Comparison of TNB among the three immune subgroups (Wilcoxon rank sum test). (B-D) Comparison of TCR diversity (B), BCR diversity (C), and RNA-seq reads mapping to VDJ loci (D) among the three immune subgroups (Wilcoxon rank sum test). (E) Heatmap showed the relative distribution of co-inhibitors (left panel) and co-stimulators (right panel) among the three immune subgroups (adjusted ANOVA). (F) Associations of HLA LOH with immune subgroups, clinicopathologic factors, and multi-omics profiles (Pearson's Chi-square-test, Fisher's exact test, or ANOVA).

Figure S7 Multi-omics features related to TLSs. (A) Associations of intra-tumoral TLSs with TLS score, immune subgroups, clinicopathologic factors, and multi-omics

profiles (ANOVA, Pearson's chi-square test, or Fisher's exact test). (B) Comparisons of xCELL enrichment scores of indicated immune subsets between TLSs- and TLSs+ subgroups (ANOVA). (C) Comparisons of calculated scores of co-inhibitors or co-stimulators between TLSs- and TLSs+ subgroups (ANOVA). (D,E) Comparison of cytolytic scores (D) and COX-IS (E) between TLSs- and TLSs+ subgroups (Wilcoxon rank sum test).

Figure S8 Influences of HBV infection on the immune microenvironment of iCCA. (A) Comparisons of HBV infection in patients of IG1 and IG2/IG3 (Fisher's exact test). (B) UMAP plot, showing the annotation and color codes for cell types in the FU-iCCA ecosystem. (C) PCA analysis of all FU-iCCA samples based on the genes exclusively enriched in IG1 and IG3. The 10 scRNA-seq samples were also projected onto the plot. (D) Dot plot of cell types assignment for indicated genes in scRNA-seq. Dot size indicated fractions of expressing cells, colored according to z-score normalized expression levels. (E,F) Bubble heatmap showing marker genes across T/NK subgroups (E) and myeloid subgroups (F) from tumor samples. Dot size indicated fraction of expressing cells, colored according to z-score normalized expression levels. (G) Immune clusters showing significant differences in the comparison among the three immune subgroups. The color saturation represented the ration to T/NK or myeloid subgroups. The *P* values were calculated by ANOVA. (H-J) Volcano plot showed differently expressed genes of CD4+ T cells (H), NK cells (I), and macrophages (J) in HBV positive versus HBV negative tumor samples.

Fig. S1

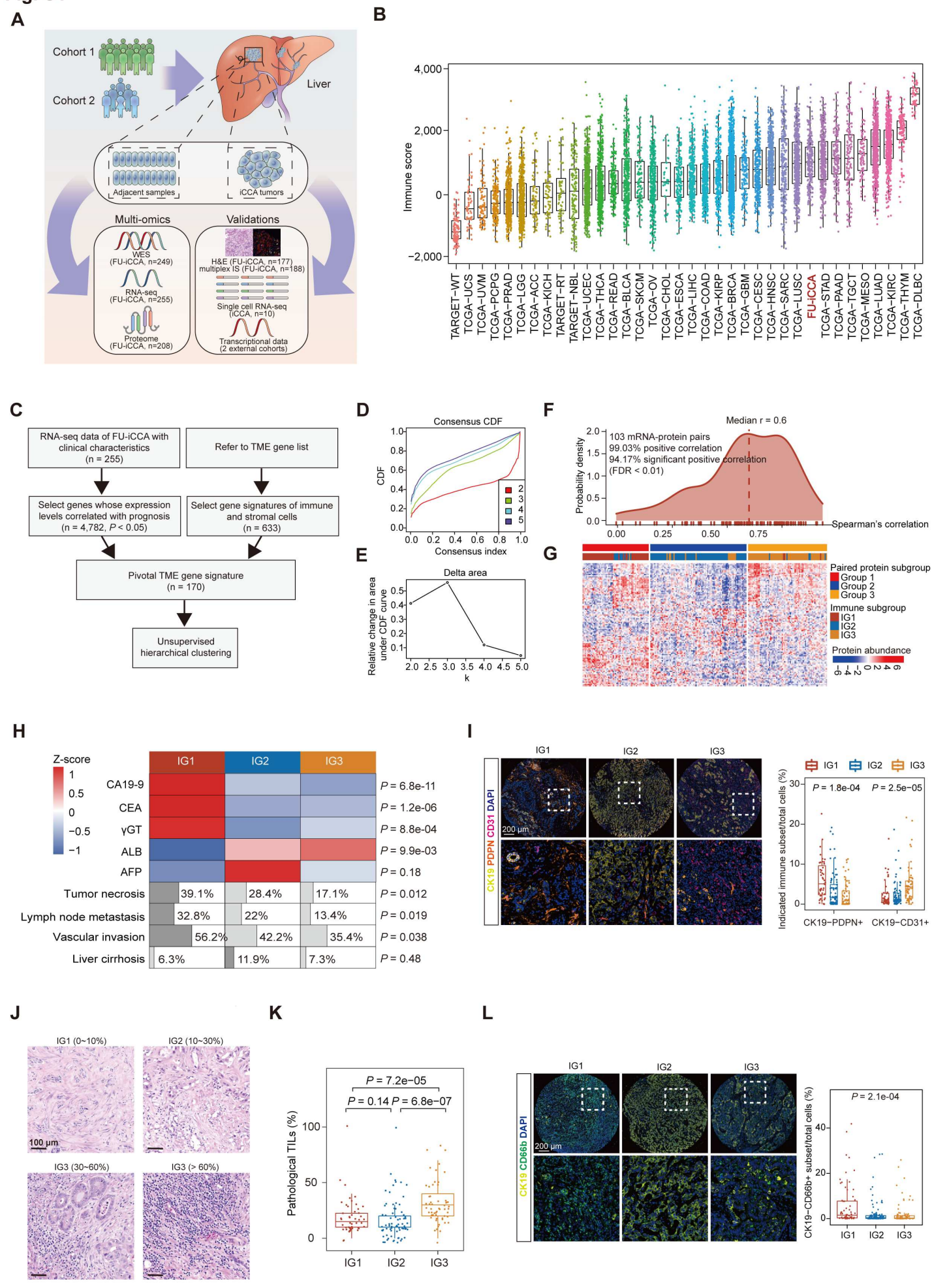
A
Cohort 1
Cohort 2
Liver
Adjacent samples
iCCA tumors
Multi-omics
Validations
WES (FU-iCCA, n=249)
RNA-seq (FU-iCCA, n=255)
Proteome (FU-iCCA, n=208)
H&E (FU-iCCA, n=177)
multiplex IS (FU-iCCA, n=188)
Single cell RNA-seq (iCCA, n=10)
Transcriptional data (2 external cohorts)
B
Immune score
TARGET-WT
TCGA-UCS
TCGA-UVM
TCGA-PCPG
TCGA-PRAD
TCGA-LGG
TCGA-ACC
TCGA-KICH
TARGET-RT
TARGET-NBL
TCGA-UCEC
TCGA-THCA
TCGA-READ
TCGA-BLCA
TCGA-SKCM
TCGA-OV
TCGA-CHOL
TCGA-ESCA
TCGA-LIHC
TCGA-COAD
TCGA-KIRP
TCGA-BRCA
TCGA-GBM
TCGA-CESC
TCGA-HNSC
TCGA-SARC
TCGA-LUSC
FU-iCCA
TCGA-STAD
TCGA-PAAD
TCGA-TGCT
TCGA-MESO
TCGA-LUAD
TCGA-KIRC
TCGA-THYM
TCGA-DLBC
C
RNA-seq data of FU-iCCA with clinical characteristics (n = 255)
Refer to TME gene list
Select genes whose expression levels correlated with prognosis (n = 4,782, P < 0.05)
Select gene signatures of immune and stromal cells (n = 633)
Pivotal TME gene signature (n = 170)
Unsupervised hierarchical clustering
D
Consensus CDF
CDF
Consensus index
E
Delta area
Relative change in area under CDF curve
k
F
Median r = 0.6
103 mRNA-protein pairs
99.03% positive correlation
94.17% significant positive correlation
(FDR < 0.01)
Probability density
Spearman's correlation
G
Paired protein subgroup
Group 1
Group 2
Group 3
Immune subgroup
IG1
IG2
IG3
Protein abundance
H
Z-score
IG1
IG2
IG3
CA19-9
CEA
γGT
ALB
AFP
Tumor necrosis
Lymph node metastasis
Vascular invasion
Liver cirrhosis
39.1%
28.4%
17.1%
32.8%
22%
13.4%
56.2%
42.2%
35.4%
6.3%
11.9%
7.3%
P = 6.8e-11
P = 1.2e-06
P = 8.8e-04
P = 9.9e-03
P = 0.18
P = 0.012
P = 0.019
P = 0.038
P = 0.48
I
IG1
IG2
IG3
CK19 PDPN CD31 DAPI
200 μm
Indicated immune subset/total cells (%)
P = 1.8e-04
P = 2.5e-05
CK19−PDPN+
CK19−CD31+
J
IG1 (0~10%)
IG2 (10~30%)
IG3 (30~60%)
IG3 (> 60%)
100 μm
K
Pathological TILs (%)
P = 7.2e−05
P = 0.14
P = 6.8e−07
L
IG1
IG2
IG3
CK19 CD66b DAPI
200 μm
CK19−CD66b+ subset/total cells (%)
P = 2.1e-04

Fig. S2

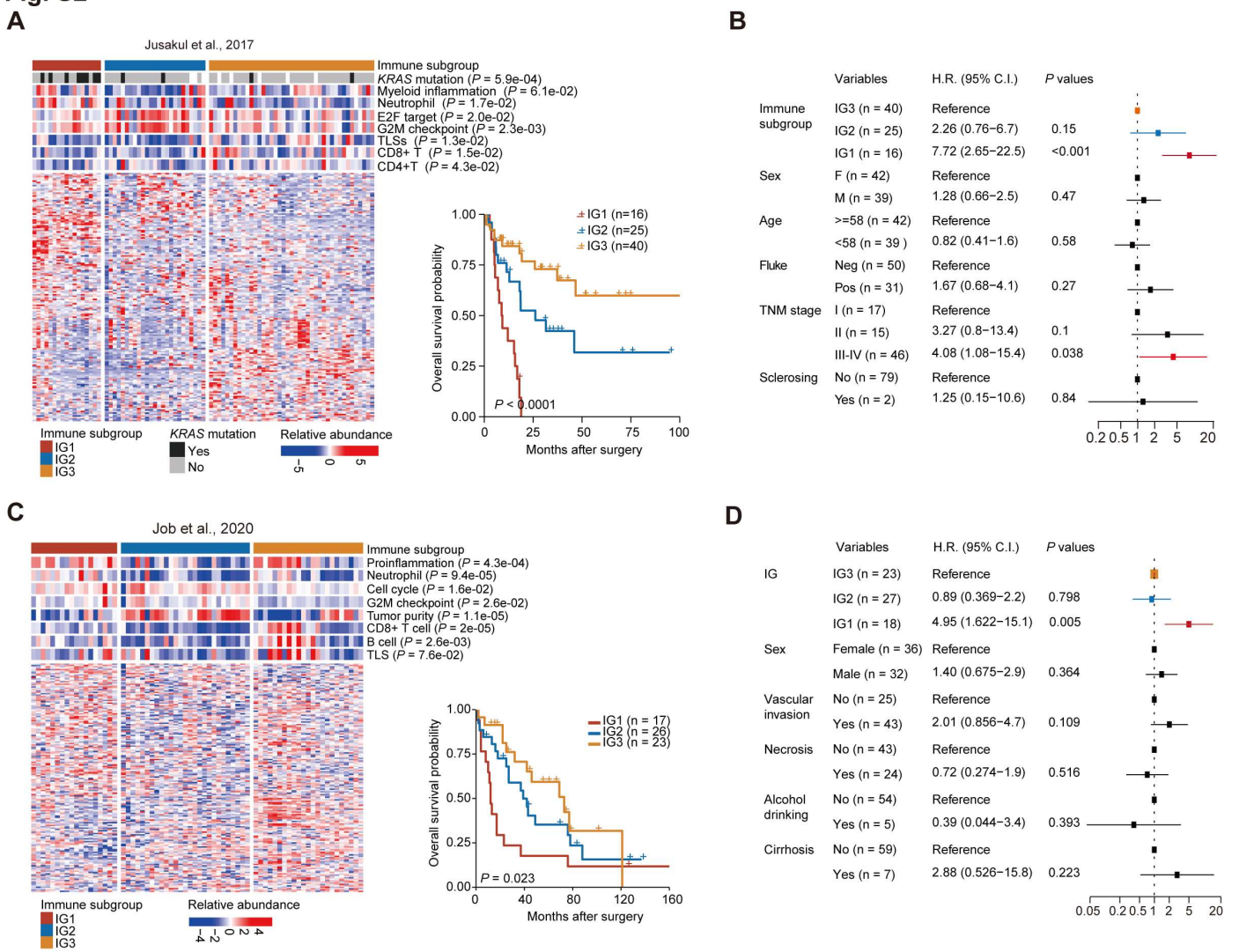
A
Jusakul et al., 2017
Immune subgroup
KRAS mutation (P = 5.9e-04)
Myeloid inflammation (P = 6.1e-02)
Neutrophil (P = 1.7e-02)
E2F target (P = 2.0e-02)
G2M checkpoint (P = 2.3e-03)
TLSs (P = 1.3e-02)
CD8+ T (P = 1.5e-02)
CD4+T (P = 4.3e-02)
Immune subgroup
IG1
IG2
IG3
KRAS mutation
Yes
No
Relative abundance
Overall survival probability
IG1 (n=16)
IG2 (n=25)
IG3 (n=40)
P < 0.0001
Months after surgery
B
Variables
H.R. (95% C.I.)
P values
Immune subgroup
IG3 (n = 40) Reference
IG2 (n = 25) 2.26 (0.76−6.7) 0.15
IG1 (n = 16) 7.72 (2.65−22.5) <0.001
Sex
F (n = 42) Reference
M (n = 39) 1.28 (0.66−2.5) 0.47
Age
>=58 (n = 42) Reference
<58 (n = 39) 0.82 (0.41−1.6) 0.58
Fluke
Neg (n = 50) Reference
Pos (n = 31) 1.67 (0.68−4.1) 0.27
TNM stage
I (n = 17) Reference
II (n = 15) 3.27 (0.8−13.4) 0.1
III-IV (n = 46) 4.08 (1.08−15.4) 0.038
Sclerosing
No (n = 79) Reference
Yes (n = 2) 1.25 (0.15−10.6) 0.84
C
Job et al., 2020
Immune subgroup
Proinflammation (P = 4.3e-04)
Neutrophil (P = 9.4e-05)
Cell cycle (P = 1.6e-02)
G2M checkpoint (P = 2.6e-02)
Tumor purity (P = 1.1e-05)
CD8+ T cell (P = 2e-05)
B cell (P = 2.6e-03)
TLS (P = 7.6e-02)
Immune subgroup
IG1
IG2
IG3
Relative abundance
Overall survival probability
IG1 (n = 17)
IG2 (n = 26)
IG3 (n = 23)
P = 0.023
Months after surgery
D
Variables
H.R. (95% C.I.)
P values
IG
IG3 (n = 23) Reference
IG2 (n = 27) 0.89 (0.369−2.2) 0.798
IG1 (n = 18) 4.95 (1.622−15.1) 0.005
Sex
Female (n = 36) Reference
Male (n = 32) 1.40 (0.675−2.9) 0.364
Vascular invasion
No (n = 25) Reference
Yes (n = 43) 2.01 (0.856−4.7) 0.109
Necrosis
No (n = 43) Reference
Yes (n = 24) 0.72 (0.274−1.9) 0.516
Alcohol drinking
No (n = 54) Reference
Yes (n = 5) 0.39 (0.044−3.4) 0.393
Cirrhosis
No (n = 59) Reference
Yes (n = 7) 2.88 (0.526−15.8) 0.223
E
FU-iCCA
Anderson
Oiishi
Sia
Job
P = 1.4e-36
P = 1.9e-28
P = 2.7e-03
P = 1.3e-08
Anderson
C1
C2
Oiishi
HpSC.like
MH.like
Sia
Inflammation
Proliferation
Job
Immunogenic
Immune desert
Myeloid
Mesenchymal
F
RNA abundance
G
RNA abundance
H
Fibroblast
HSCactivated
Myofibroblast
B derived
Cytotoxic
Monocyte derived
Myeloid
HSCquiescent
Lymphoid
NK or T
T adaptative
Complement
Proinflammation
Checkpoint
Relative abundance

Fig. S3

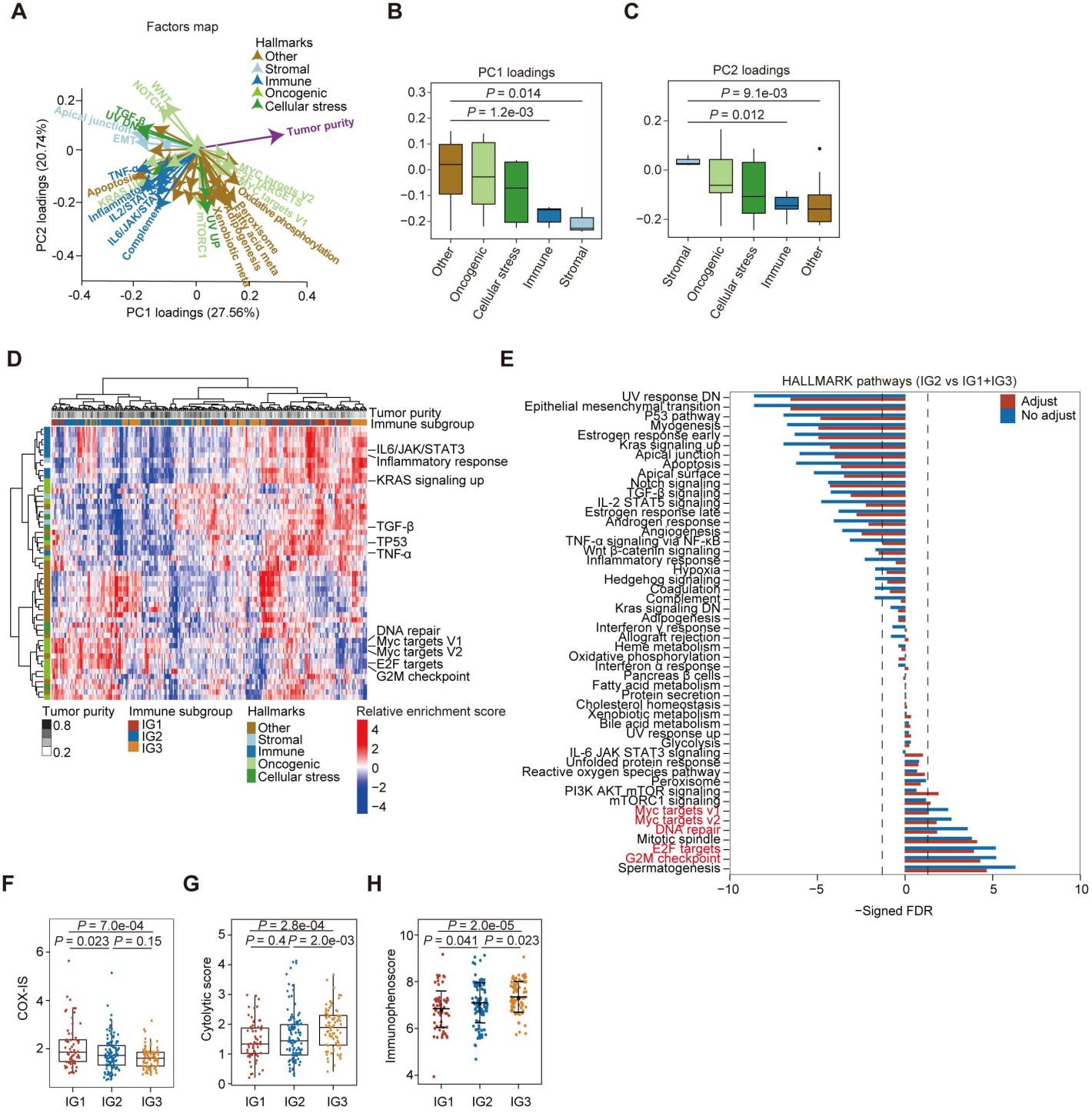
A
Factors map
Hallmarks
Other
Stromal
Immune
Oncogenic
Cellular stress
Tumor purity
PC2 loadings (20.74%)
PC1 loadings (27.56%)
B
PC1 loadings
P = 0.014
P = 1.2e-03
Other
Oncogenic
Cellular stress
Immune
Stromal
C
PC2 loadings
P = 9.1e-03
P = 0.012
Stromal
Oncogenic
Cellular stress
Immune
Other
D
Tumor purity
Immune subgroup
IL6/JAK/STAT3
Inflammatory response
KRAS signaling up
TGF-β
TP53
TNF-α
DNA repair
Myc targets V1
Myc targets V2
E2F targets
G2M checkpoint
Tumor purity
0.8
0.2
Immune subgroup
IG1
IG2
IG3
Hallmarks
Other
Stromal
Immune
Oncogenic
Cellular stress
Relative enrichment score
4
2
0
−2
−4
E
HALLMARK pathways (IG2 vs IG1+IG3)
Adjust
No adjust
UV response DN
Epithelial mesenchymal transition
P53 pathway
Myogenesis
Estrogen response early
Kras signaling up
Apical junction
Apoptosis
Apical surface
Notch signaling
TGF-β signaling
IL-2 STAT5 signaling
Estrogen response late
Androgen response
Angiogenesis
TNF-α signaling via NF-κB
Wnt β-catenin signaling
Inflammatory response
Hypoxia
Hedgehog signaling
Coagulation
Complement
Kras signaling DN
Adipogenesis
Interferon γ response
Allograft rejection
Heme metabolism
Oxidative phosphorylation
Interferon α response
Pancreas β cells
Fatty acid metabolism
Protein secretion
Cholesterol homeostasis
Xenobiotic metabolism
Bile acid metabolism
UV response up
Glycolysis
IL-6 JAK STAT3 signaling
Unfolded protein response
Reactive oxygen species pathway
Peroxisome
PI3K AKT mTOR signaling
mTORC1 signaling
Myc targets v1
Myc targets v2
DNA repair
Mitotic spindle
E2F targets
G2M checkpoint
Spermatogenesis
−10
−5
0
5
10
−Signed FDR
F
P = 7.0e-04
P = 0.023
P = 0.15
COX-IS
IG1
IG2
IG3
G
P = 2.8e-04
P = 0.4
P = 2.0e-03
Cytolytic score
IG1
IG2
IG3
H
P = 2.0e-05
P = 0.041
P = 0.023
Immunophenoscore
IG1
IG2
IG3

Fig. S4

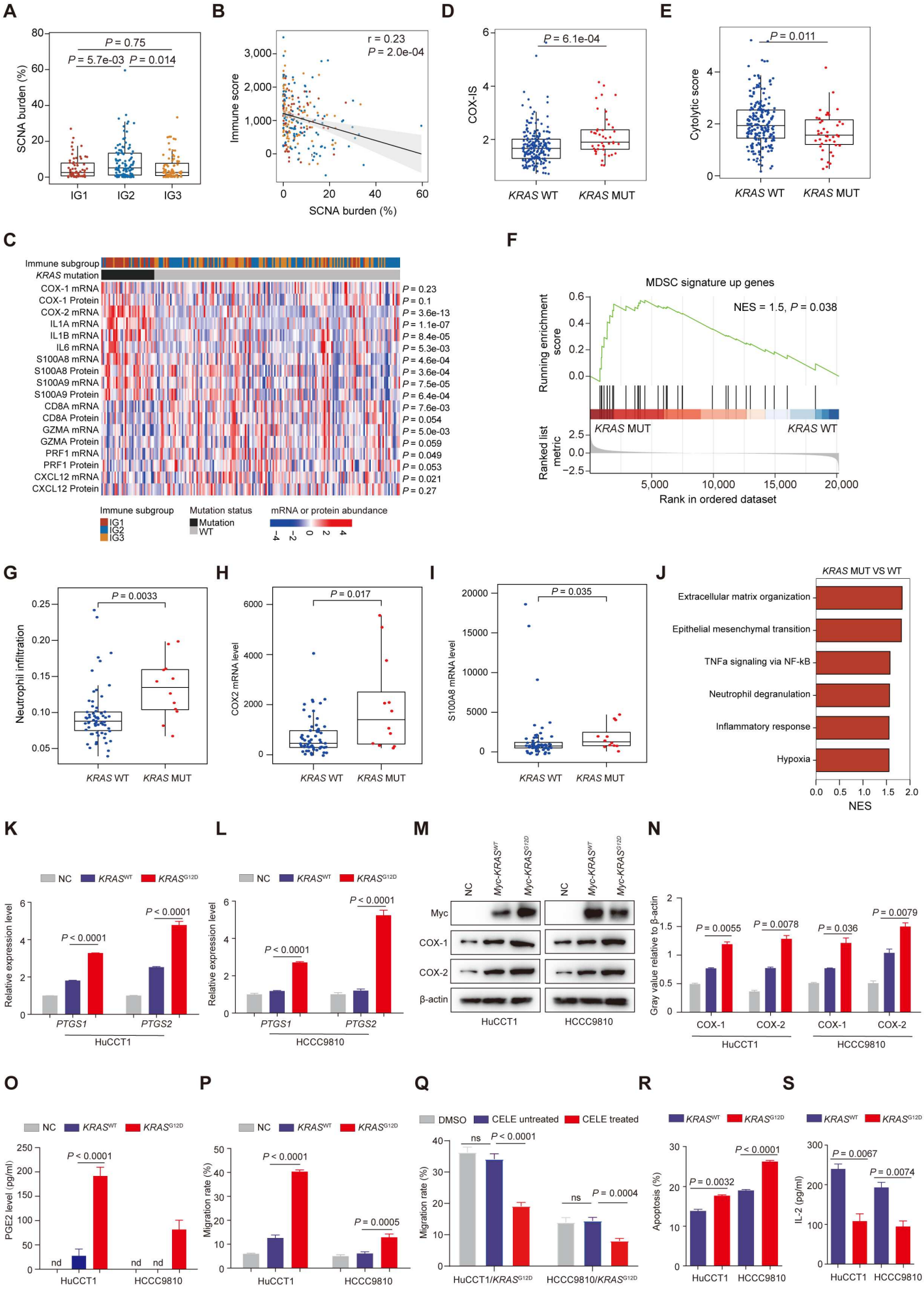
A
SCNA burden (%)
P = 0.75
P = 5.7e-03
P = 0.014
IG1
IG2
IG3
B
Immune score
r = 0.23
P = 2.0e-04
SCNA burden (%)
D
COX-IS
P = 6.1e-04
KRAS WT
KRAS MUT
E
Cytolytic score
P = 0.011
KRAS WT
KRAS MUT
C
Immune subgroup
KRAS mutation
COX-1 mRNA P = 0.23
COX-1 Protein P = 0.1
COX-2 mRNA P = 3.6e-13
IL1A mRNA P = 1.1e-07
IL1B mRNA P = 8.4e-05
IL6 mRNA P = 5.3e-03
S100A8 mRNA P = 4.6e-04
S100A8 Protein P = 3.6e-04
S100A9 mRNA P = 7.5e-05
S100A9 Protein P = 6.4e-04
CD8A mRNA P = 7.6e-03
CD8A Protein P = 0.054
GZMA mRNA P = 5.0e-03
GZMA Protein P = 0.059
PRF1 mRNA P = 0.049
PRF1 Protein P = 0.053
CXCL12 mRNA P = 0.021
CXCL12 Protein P = 0.27
Immune subgroup
IG1
IG2
IG3
Mutation status
Mutation
WT
mRNA or protein abundance
F
MDSC signature up genes
NES = 1.5, P = 0.038
Running enrichment score
KRAS MUT
KRAS WT
Ranked list metric
Rank in ordered dataset
G
Neutrophil infiltration
P = 0.0033
KRAS WT
KRAS MUT
H
COX2 mRNA level
P = 0.017
KRAS WT
KRAS MUT
I
S100A8 mRNA level
P = 0.035
KRAS WT
KRAS MUT
J
KRAS MUT VS WT
Extracellular matrix organization
Epithelial mesenchymal transition
TNFa signaling via NF-kB
Neutrophil degranulation
Inflammatory response
Hypoxia
NES
K
NC
KRASWT
KRASG12D
Relative expression level
P < 0.0001
P < 0.0001
P < 0.0001
PTGS1
PTGS2
HuCCT1
L
NC
KRASWT
KRASG12D
Relative expression level
P < 0.0001
P < 0.0001
PTGS1
PTGS2
HCCC9810
M
NC
Myc-KRASWT
Myc-KRASG12D
NC
Myc-KRASWT
Myc-KRASG12D
Myc
COX-1
COX-2
β-actin
HuCCT1
HCCC9810
N
Gray value relative to β-actin
P = 0.0055
P = 0.0078
P = 0.036
P = 0.0079
COX-1
COX-2
COX-1
COX-2
HuCCT1
HCCC9810
O
NC
KRASWT
KRASG12D
PGE2 level (pg/ml)
P < 0.0001
nd
nd
nd
HuCCT1
HCCC9810
P
NC
KRASWT
KRASG12D
Migration rate (%)
P < 0.0001
P = 0.0005
HuCCT1
HCCC9810
Q
DMSO
CELE untreated
CELE treated
Migration rate (%)
ns
P < 0.0001
ns
P = 0.0004
HuCCT1/KRASG12D
HCCC9810/KRASG12D
R
KRASWT
KRASG12D
Apoptosis (%)
P = 0.0032
P < 0.0001
HuCCT1
HCCC9810
S
KRASWT
KRASG12D
IL-2 (pg/ml)
P = 0.0067
P = 0.0074
HuCCT1
HCCC9810

Fig. S5

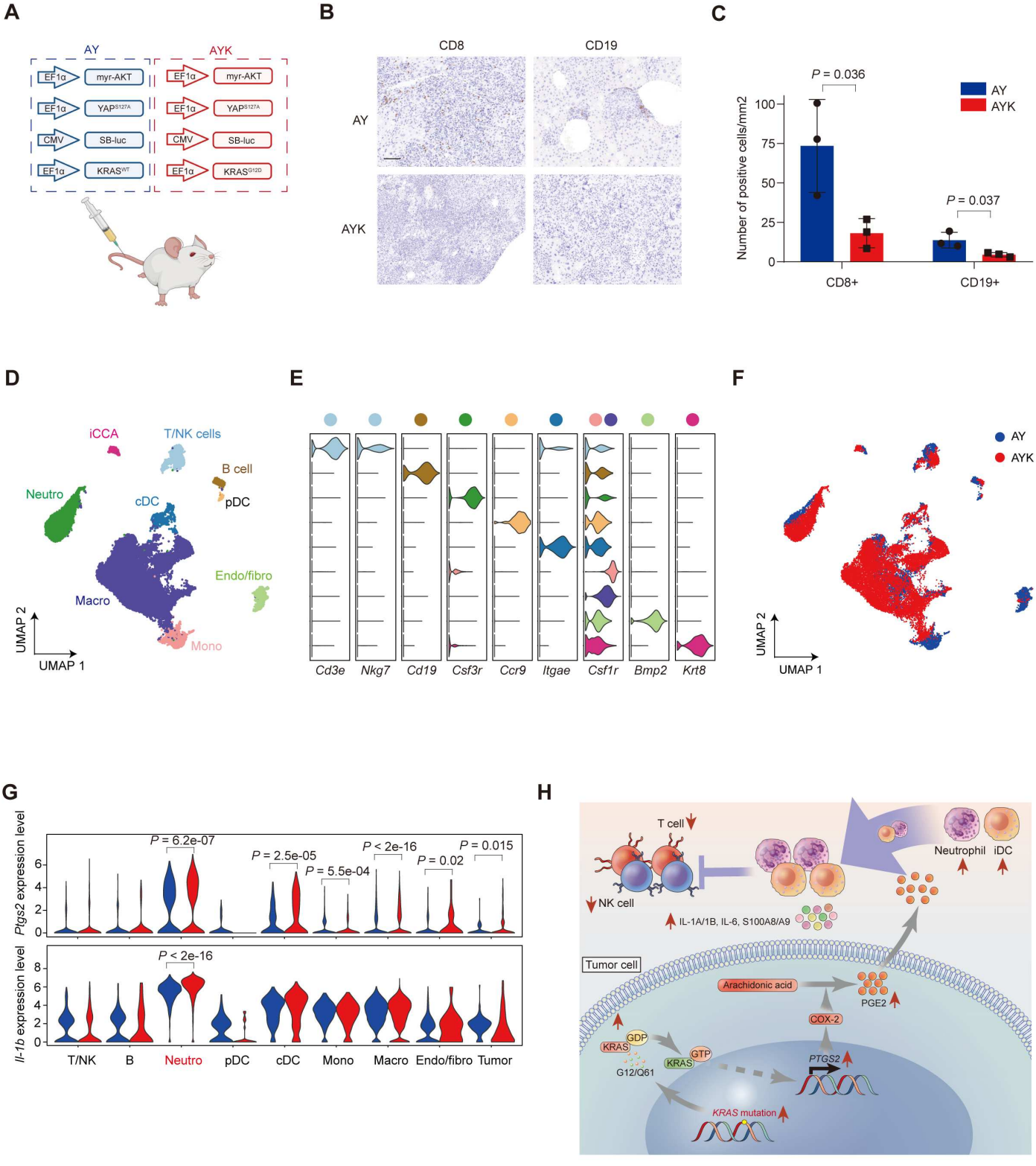
A
AY
AYK
EF1α
myr-AKT
YAP^S127A
CMV
SB-luc
KRAS^WT
KRAS^G12D
B
CD8
CD19
AY
AYK
C
P = 0.036
P = 0.037
AY
AYK
Number of positive cells/mm2
100
75
50
25
0
CD8+
CD19+
D
iCCA
T/NK cells
B cell
Neutro
cDC
pDC
Endo/fibro
Macro
Mono
UMAP 2
UMAP 1
E
Cd3e
Nkg7
Cd19
Csf3r
Ccr9
Itgae
Csf1r
Bmp2
Krt8
F
AY
AYK
UMAP 2
UMAP 1
G
Ptgs2 expression level
P = 6.2e-07
P = 2.5e-05
P = 5.5e-04
P < 2e-16
P = 0.02
P = 0.015
Il-1b expression level
P < 2e-16
T/NK
B
Neutro
pDC
cDC
Mono
Macro
Endo/fibro
Tumor
H
T cell
NK cell
Neutrophil
iDC
IL-1A/1B, IL-6, S100A8/A9
Tumor cell
Arachidonic acid
PGE2
COX-2
KRAS
GDP
GTP
G12/Q61
PTGS2
KRAS mutation

Fig. S6

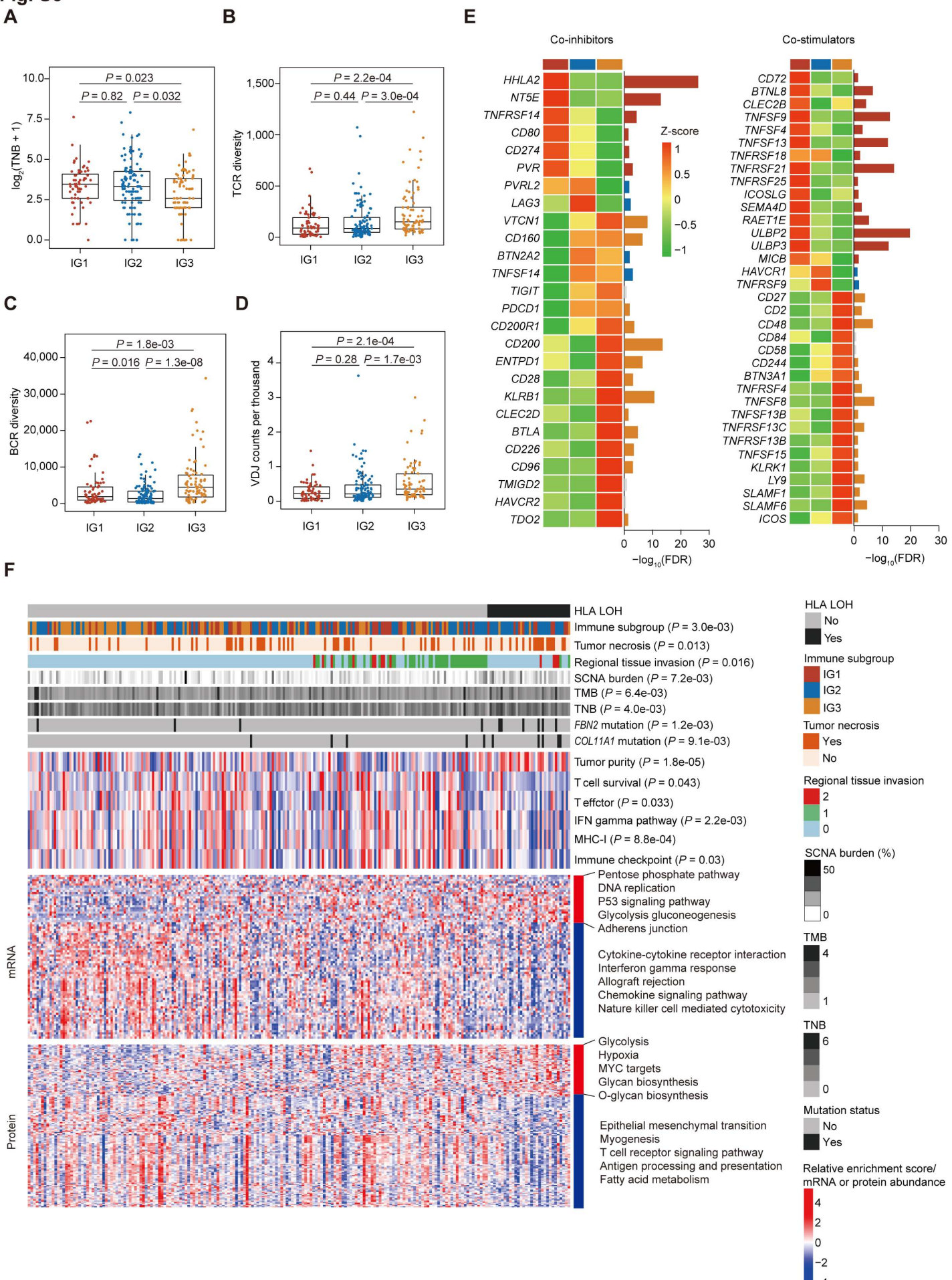
A
log2(TNB + 1)
P = 0.023
P = 0.82
P = 0.032
IG1
IG2
IG3
B
TCR diversity
P = 2.2e-04
P = 0.44
P = 3.0e-04
C
BCR diversity
P = 1.8e-03
P = 0.016
P = 1.3e-08
D
VDJ counts per thousand
P = 2.1e-04
P = 0.28
P = 1.7e-03
E
Co-inhibitors
HHLA2
NT5E
TNFRSF14
CD80
CD274
PVR
PVRL2
LAG3
VTCN1
CD160
BTN2A2
TNFSF14
TIGIT
PDCD1
CD200R1
CD200
ENTPD1
CD28
KLRB1
CLEC2D
BTLA
CD226
CD96
TMIGD2
HAVCR2
TDO2
Z-score
−log10(FDR)
Co-stimulators
CD72
BTNL8
CLEC2B
TNFSF9
TNFSF4
TNFSF13
TNFRSF18
TNFRSF21
TNFRSF25
ICOSLG
SEMA4D
RAET1E
ULBP2
ULBP3
MICB
HAVCR1
TNFRSF9
CD27
CD2
CD48
CD84
CD58
CD244
BTN3A1
TNFRSF4
TNFSF8
TNFSF13B
TNFRSF13C
TNFRSF13B
TNFSF15
KLRK1
LY9
SLAMF1
SLAMF6
ICOS
F
HLA LOH
Immune subgroup (P = 3.0e-03)
Tumor necrosis (P = 0.013)
Regional tissue invasion (P = 0.016)
SCNA burden (P = 7.2e-03)
TMB (P = 6.4e-03)
TNB (P = 4.0e-03)
FBN2 mutation (P = 1.2e-03)
COL11A1 mutation (P = 9.1e-03)
Tumor purity (P = 1.8e-05)
T cell survival (P = 0.043)
T effctor (P = 0.033)
IFN gamma pathway (P = 2.2e-03)
MHC-I (P = 8.8e-04)
Immune checkpoint (P = 0.03)
mRNA
Protein
Pentose phosphate pathway
DNA replication
P53 signaling pathway
Glycolysis gluconeogenesis
Adherens junction
Cytokine-cytokine receptor interaction
Interferon gamma response
Allograft rejection
Chemokine signaling pathway
Nature killer cell mediated cytotoxicity
Glycolysis
Hypoxia
MYC targets
Glycan biosynthesis
O-glycan biosynthesis
Epithelial mesenchymal transition
Myogenesis
T cell receptor signaling pathway
Antigen processing and presentation
Fatty acid metabolism
HLA LOH
No
Yes
Immune subgroup
IG1
IG2
IG3
Tumor necrosis
Yes
No
Regional tissue invasion
SCNA burden (%)
TMB
TNB
Mutation status
Relative enrichment score/
mRNA or protein abundance

Fig. S7

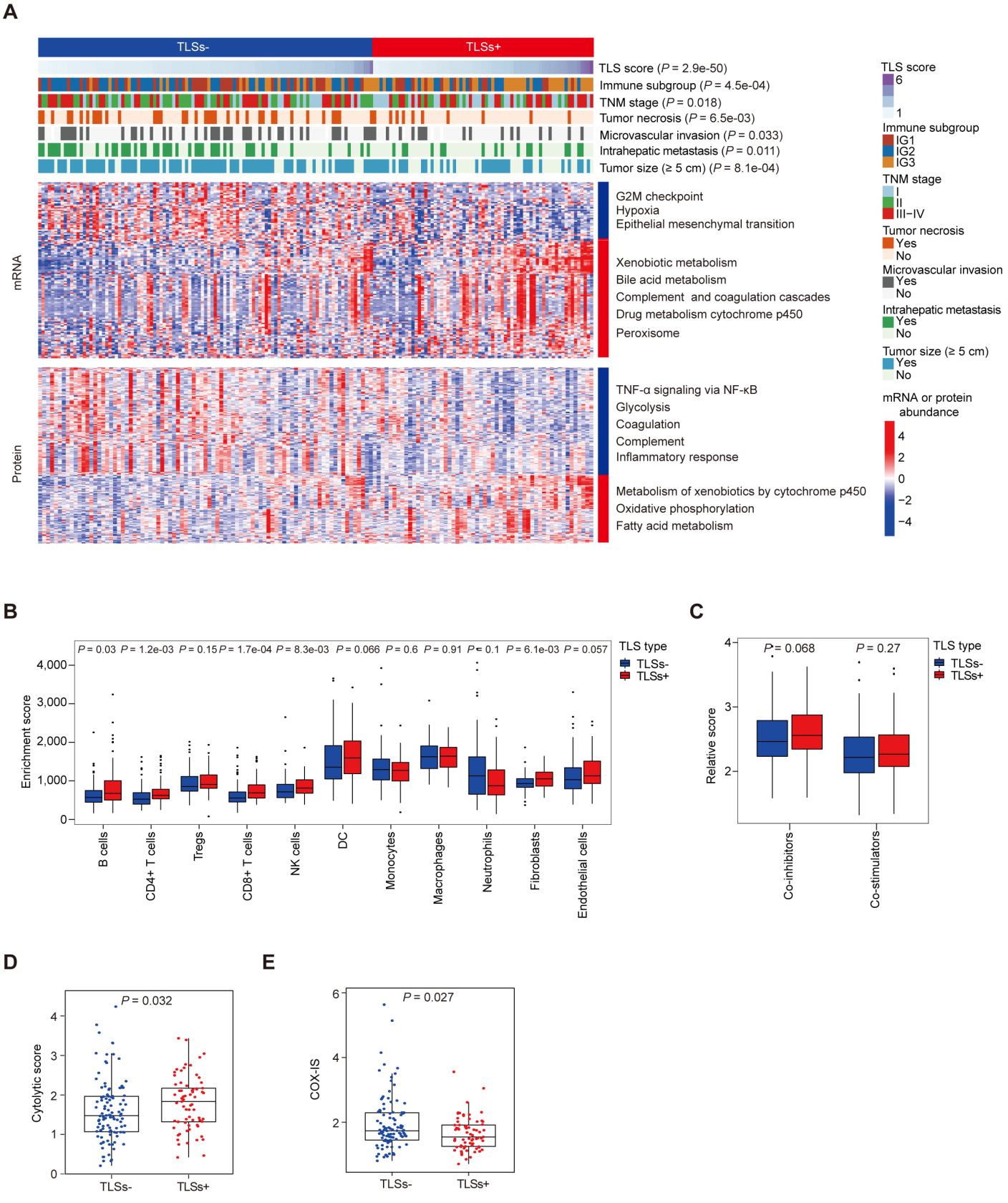
A
TLSs-
TLSs+
TLS score (P = 2.9e-50)
Immune subgroup (P = 4.5e-04)
TNM stage (P = 0.018)
Tumor necrosis (P = 6.5e-03)
Microvascular invasion (P = 0.033)
Intrahepatic metastasis (P = 0.011)
Tumor size (≥ 5 cm) (P = 8.1e-04)
mRNA
Protein
G2M checkpoint
Hypoxia
Epithelial mesenchymal transition
Xenobiotic metabolism
Bile acid metabolism
Complement and coagulation cascades
Drug metabolism cytochrome p450
Peroxisome
TNF-α signaling via NF-κB
Glycolysis
Coagulation
Complement
Inflammatory response
Metabolism of xenobiotics by cytochrome p450
Oxidative phosphorylation
Fatty acid metabolism
TLS score
6
1
Immune subgroup
IG1
IG2
IG3
TNM stage
I
II
III−IV
Tumor necrosis
Yes
No
Microvascular invasion
Yes
No
Intrahepatic metastasis
Yes
No
Tumor size (≥ 5 cm)
Yes
No
mRNA or protein abundance
4
2
0
−2
−4
B
P = 0.03 P = 1.2e-03 P = 0.15 P = 1.7e-04 P = 8.3e-03 P = 0.066 P = 0.6 P = 0.91 P = 0.1 P = 6.1e-03 P = 0.057
Enrichment score
4,000
3,000
2,000
1,000
0
TLS type
TLSs-
TLSs+
B cells
CD4+ T cells
Tregs
CD8+ T cells
NK cells
DC
Monocytes
Macrophages
Neutrophils
Fibroblasts
Endothelial cells
C
P = 0.068
P = 0.27
Relative score
4
3
2
TLS type
TLSs-
TLSs+
Co-inhibitors
Co-stimulators
D
P = 0.032
Cytolytic score
4
3
2
1
0
TLSs-
TLSs+
E
P = 0.027
COX-IS
6
4
2
TLSs-
TLSs+

Fig. S8

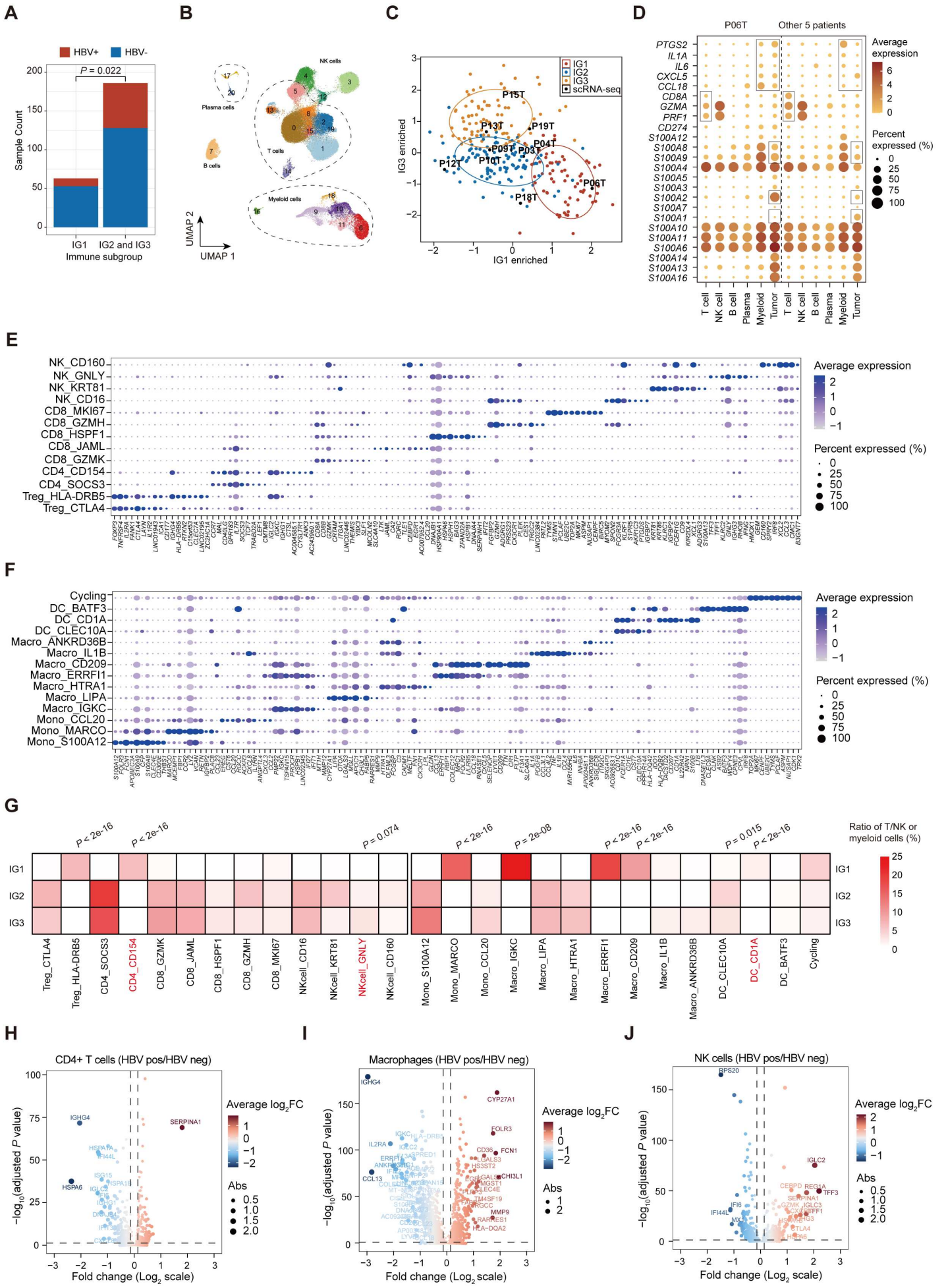
A
HBV+
HBV-
P = 0.022
Sample Count
Immune subgroup
IG1
IG2 and IG3
B
NK cells
Plasma cells
T cells
B cells
Myeloid cells
UMAP 2
UMAP 1
C
IG1
IG2
IG3
scRNA-seq
IG3 enriched
IG1 enriched
P15T
P13T
P19T
P09T
P03T
P04T
P12T
P10T
P06T
P18T
D
P06T
Other 5 patients
Average expression
Percent expressed (%)
PTGS2
IL1A
IL6
CXCL5
CCL18
CD8A
GZMA
PRF1
CD274
S100A12
S100A8
S100A9
S100A4
S100A5
S100A3
S100A2
S100A7
S100A1
S100A10
S100A11
S100A6
S100A14
S100A13
S100A16
T cell
NK cell
B cell
Plasma
Myeloid
Tumor
E
NK_CD160
NK_GNLY
NK_KRT81
NK_CD16
CD8_MKI67
CD8_GZMH
CD8_HSPF1
CD8_JAML
CD8_GZMK
CD4_CD154
CD4_SOCS3
Treg_HLA-DRB5
Treg_CTLA4
Average expression
Percent expressed (%)
F
Cycling
DC_BATF3
DC_CD1A
DC_CLEC10A
Macro_ANKRD36B
Macro_IL1B
Macro_CD209
Macro_ERRFI1
Macro_HTRA1
Macro_LIPA
Macro_IGKC
Mono_CCL20
Mono_MARCO
Mono_S100A12
Average expression
Percent expressed (%)
G
P < 2e-16
P < 2e-16
P = 0.074
P < 2e-16
P = 2e-08
P < 2e-16
P < 2e-16
P = 0.015
P < 2e-16
Ratio of T/NK or myeloid cells (%)
IG1
IG2
IG3
Treg_CTLA4
Treg_HLA-DRB5
CD4_SOCS3
CD4_CD154
CD8_GZMK
CD8_JAML
CD8_HSPF1
CD8_GZMH
CD8_MKI67
NKcell_CD16
NKcell_KRT81
NKcell_GNLY
NKcell_CD160
Mono_S100A12
Mono_MARCO
Mono_CCL20
Macro_IGKC
Macro_LIPA
Macro_HTRA1
Macro_ERRFI1
Macro_CD209
Macro_IL1B
Macro_ANKRD36B
DC_CLEC10A
DC_CD1A
DC_BATF3
Cycling
H
CD4+ T cells (HBV pos/HBV neg)
IGHG4
SERPINA1
HSPA6
−log10(adjusted P value)
Fold change (Log2 scale)
Average log2FC
Abs
I
Macrophages (HBV pos/HBV neg)
IGHG4
CYP27A1
FOLR3
IL2RA
CD36
FCN1
CCL13
CHI3L1
MMP9
RARRES1
HLA-DQA2
−log10(adjusted P value)
Fold change (Log2 scale)
Average log2FC
Abs
J
NK cells (HBV pos/HBV neg)
RPS20
IGLC2
TFF3
REG1A
IFI6
IFI44L
MX1
−log10(adjusted P value)
Fold change (Log2 scale)
Average log2FC
Abs